EFDA–JET–PR(11)45

J. Citrin, J. Hobirk, M. Schneider, J.F. Artaud, C. Bourdelle, K. Crombe,
G.M.D. Hogeweij, F. Imbeaux, E. Joffrin, F. Koechl, J. Stober,
ASDEX Upgrade team, ITM-TF ITER Scenario Modelling group
and JET EFDA contributors

Predictive Analysis of q-profile Influence on Transport in JET and AUG Hybrid Scenarios

Predictive Analysis of q-profile Influence on Transport in JET and AUG Hybrid Scenarios

J. Citrin[1], J. Hobirk[2], M. Schneider[3], J.F. Artaud[3], C. Bourdelle[3], K. Crombe[4], G.M.D. Hogeweij[1], F. Imbeaux[3], E. Joffrin[3], F. Koechl[5], J. Stober[2], ASDEX Upgrade team, ITM-TF ITER Scenario Modelling group and JET EFDA contributors*

JET-EFDA, Culham Science Centre, OX14 3DB, Abingdon, UK

[1]FOM Institute for Plasma Physics Rijnhuizen, Association EURATOM-FOM, Nieuwegein, The Netherlands
[2]MPI für Plasmaphysik, EURATOM Assoc., Boltzmannstr. 2, 85748 Garching, Germany
[3]CEA, IRFM, F-13108 Saint Paul Lez Durance, France
[4]Department of Applied Physics, Ghent University, Rozier 44, 9000 Ghent, Belgium
[5]Association EURATOM-ÖAW/ATI, Atominstitut, TU Wien, 1020 Vienna, Austria
** See annex of F. Romanelli et al, "Overview of JET Results", (23rd IAEA Fusion Energy Conference, Daejon, Republic of Korea (2010)).*

Preprint of Paper to be submitted for publication in Plasma Physics and Controlled Fusion

ABSTRACT.
Hybrid scenarios in present machines are characterized by improved confinement compared to the IPB98(y,2) empirical scaling law expectations. This work concentrates on isolating the impact of increased s/q at outer radii (where s is the magnetic shear) on core confinement in low-triangularity JET and ASDEX Upgrade (AUG) experiments. This is carried out by predictive heat and particle transport modelling using the integrated modelling code CRONOS coupled to the GLF23 turbulent transport model. For both machines, discharge pairs were analyzed displaying similar pedestal confinement yet significant differences in core confinement. From these comparisons, it is found that s/q shaping at outer radii may be responsible for up to 1 50% of the relative core confinement improvement observed in these specific discharges. This relative improvement is independent of the degree of rotational shear turbulence suppression assumed in the GLF23 model. However, employing the full GLF23 rotational shear model leads to an overprediction of the ion temperatures in all discharges analyzed. Additional mechanisms for core confinement improvement are discussed and estimated. Further linear threshold analysis with QuaLiKiz is carried out on both pairs of discharges. This work aims to validate recent predictions of the ITER hybrid scenario also employing CRONOS/GLF23, where a high level of confinement and resultant fusion power sensitivity to the s/q profile was found.

1. Introduction

Over the past decade, an attractive operating scenario for the ITER tokamak has emerged, combining long discharge times similar to the steady-state scenario, while maintaining the reliability of the reference H-mode scenario. This so-called 'hybrid' scenario aims to maximize neutron fluence per shot by achieving an extended burn time ($t > 1000\ s$ in ITER) together with significant α-particle heating ($Q > 5$) [1]. The extended burn time is achieved by operation at reduced current and at a higher non-inductive current fraction compared to the reference H-mode scenario. The basis for this scenario has been established at DIII-D [2], AUG ('improved H-modes') [3], JET [4] and JT-60 [5].

In present tokamaks, the hybrid scenario is characterized by a q-profile maintained close to but above unity, with a broad region of low magnetic shear. The lack of deleterious NTM triggering sawteeth, due to $q > 1$, thus allows operation at a β_N higher than in sawtoothing discharges. These discharges frequently display improved confinement compared to the IPB98(y,2) empirical scaling law expectations, with H_{98} in the range of $1 - 1.5$. $H_{98} \equiv \tau_{th}/\tau_{IPB98(y,2)}$, where τ_{th} is the thermal confinement time and $\tau_{IPB98(y,2)}$ the empirical scaling law confinement time introduced in [6]. Assuming the same H_{98} factor as in present experiments, this performance extrapolates favourably in ITER, beyond the minimum $Q = 5$ ITER hybrid scenario requirement [7, 8, 9]. It is clearly of great importance to understand the source of improved confinement in present machines, to reliably extrapolate the scenario to ITER.

A number of possibilities explaining the confinement improvement have been proposed. Pedestal confinement improvement due to an increase of pedestal width

with β_N is reported in AUG improved H-modes [10, 11]. In JET, the β_N confinement scaling has been observed to depend on triangularity [12]. Low triangularity discharges display a weak β_N dependence and thus higher H_{98} at high β_N. One should note that the IPB98(y,2) scaling law was developed for discharges primarily in the range $\beta_N = 1 - 2$, lower than most hybrid discharges.

Improved core confinement is seen in DIII-D hybrids and 'late-heating' AUG improved H-mode discharges, with electromagnetic gyrokinetic calculations showing that β-stabilization may be responsible for the core confinement improvement [11]. Rotation is seen to play an important role in improved confinement. Variable torque experiments at DIII-D by simultaneous application of co and counter beams led to a decrease of H_{98} from 1.5 to 1.1 in the extreme low rotation case (central $M \approx 0.15$) [13]. However, this H_{98} factor is still as high as in high rotation conventional H-mode plasmas, showing that further factors are also responsible for core confinement improvement. The precise mechanism of rotational shear core confinement improvement is also currently under investigation. Observations at JET point to the combination of low magnetic shear and high rotational shear leading to significantly reduced ion temperature profile stiffness [14, 15]. This is in opposition to the instability threshold offset observed in non-linear simulations and reproduced in reduced models such as GLF23 [16], which describe well the effect of rotation particularly for DIII-D [13]. Finally, the characteristic hybrid scenario q-profile shape - a central broad region of low magnetic shear, and increased magnetic shear towards the edge - may further contribute to improved confinement through a relative increase in s/q at outer radii, leading to an increase in the ITG threshold. This can be seen from the ITG threshold linear gyrokinetic analytical expression, in the flat density limit [17]:

$$(R/L_{Ti})_{crit} = \frac{4}{3}(1 + T_i/T_e)(1 + 2\frac{s}{q}), \quad with\ R/L_n < 2(1 + T_i/T_e) \tag{1}$$

A similar dependency in the collisionless, flat density limit with both passing and trapped electrons was reported in modelling carried out with the Kinezero linear gyrokinetic code [18]. For $s > 0$ and for $T_i/T_e = 1$, the best fit of R/L_{Ti} following parameter scans in s and q was found as [19]:

$$(R/L_{Ti})_{crit} = 2(1.1 + 1.4s + 1.9\frac{s}{q}) \tag{2}$$

Similar s/q dependence has also been observed in electron heat transport experiments on Tore Supra [20, 21].

This work concentrates on isolating the impact of varying s/q at outer radii on core confinement in *low-triangularity* JET and AUG hybrid scenario experiments. For each machine, a pair of shots has been chosen which display a similar level of pedestal confinement yet a significant difference in core confinement. For each pair, the improved confinement case corresponds to a higher average s/q parameter. The aim of this work is to assess whether the predicted threshold improvement due to q-profile shaping is consistent with the observations. This is carried out by predictive heat and particle transport modelling using the integrated modelling code CRONOS [22] coupled to the

with β_N is reported in AUG improved H-modes [10, 11]. In JET, the β_N confinement scaling has been observed to depend on triangularity [12]. Low triangularity discharges display a weak β_N dependence and thus higher H_{98} at high β_N. One should note that the IPB98(y,2) scaling law was developed for discharges primarily in the range $\beta_N = 1 - 2$, lower than most hybrid discharges.

Improved core confinement is seen in DIII-D hybrids and 'late-heating' AUG improved H-mode discharges, with electromagnetic gyrokinetic calculations showing that β-stabilization may be responsible for the core confinement improvement [11]. Rotation is seen to play an important role in improved confinement. Variable torque experiments at DIII-D by simultaneous application of co and counter beams led to a decrease of H_{98} from 1.5 to 1.1 in the extreme low rotation case (central $M \approx 0.15$) [13]. However, this H_{98} factor is still as high as in high rotation conventional H-mode plasmas, showing that further factors are also responsible for core confinement improvement. The precise mechanism of rotational shear core confinement improvement is also currently under investigation. Observations at JET point to the combination of low magnetic shear and high rotational shear leading to significantly reduced ion temperature profile stiffness [14, 15]. This is in opposition to the instability threshold offset observed in non-linear simulations and reproduced in reduced models such as GLF23 [16], which describe well the effect of rotation particularly for DIII-D [13]. Finally, the characteristic hybrid scenario q-profile shape - a central broad region of low magnetic shear, and increased magnetic shear towards the edge - may further contribute to improved confinement through a relative increase in s/q at outer radii, leading to an increase in the ITG threshold. This can be seen from the ITG threshold linear gyrokinetic analytical expression, in the flat density limit [17]:

$$(R/L_{Ti})_{crit} = \frac{4}{3}(1 + T_i/T_e)(1 + 2\frac{s}{q}), \quad with\ R/L_n < 2(1 + T_i/T_e) \tag{1}$$

A similar dependency in the collisionless, flat density limit with both passing and trapped electrons was reported in modelling carried out with the Kinezero linear gyrokinetic code [18]. For $s > 0$ and for $T_i/T_e = 1$, the best fit of R/L_{Ti} following parameter scans in s and q was found as [19]:

$$(R/L_{Ti})_{crit} = 2(1.1 + 1.4s + 1.9\frac{s}{q}) \tag{2}$$

Similar s/q dependence has also been observed in electron heat transport experiments on Tore Supra [20, 21].

This work concentrates on isolating the impact of varying s/q at outer radii on core confinement in *low-triangularity* JET and AUG hybrid scenario experiments. For each machine, a pair of shots has been chosen which display a similar level of pedestal confinement yet a significant difference in core confinement. For each pair, the improved confinement case corresponds to a higher average s/q parameter. The aim of this work is to assess whether the predicted threshold improvement due to q-profile shaping is consistent with the observations. This is carried out by predictive heat and particle transport modelling using the integrated modelling code CRONOS [22] coupled to the

GLF23 turbulent transport model [16, 23]. Successful validation of the GLF23 q-profile scaling has been carried out on DIII-D discharges at fixed magnetic shear [24]. The GLF23 modelling is supplemented by linear instability threshold calculations with the linear gyrokinetic code QuaLiKiz [25], based on the Kinezero code. One of the driving motivations of this work is to validate recent predictions of the ITER hybrid scenario also employing CRONOS/GLF23, where a high level of fusion power sensitivity to the s/q profile was found, even for relatively modest improvements in H_{98} [26].

This paper is organized as follows: the experimental discharges are described in section 2, the modelling tools and techniques in section 3, the GLF23 modelling results in section 4, additional mechanisms for core confinement improvement are discussed in section 5, the QuaLiKiz results in section 6, and the discussion and conclusions in section 7.

2. Experimental discharges

For both machines, discharge pairs were analyzed displaying similar pedestal confinement yet significant differences in core confinement. A variation in q-profile was experimentally achieved in each pair. For the JET pair (79626/79630), this variation was achieved via the 'current-overshoot' method [27, 9]. With this method, the current is ramped down to its flat-top value just prior to the main heating phase, resulting in a broader q-profile compared with a regular ramp-up scenario. For the AUG pair (20993/20995), the q-profile variation was achieved by varying the auxiliary heating timing, with the later heating case resulting in a broader q-profile [28]. Apart from the abovementioned variations, all other control parameters (e.g. shaping, fueling, total heating power) are kept the same between the discharges of each pair. The total flattop P_{aux} for the JET case is $\approx 17MW$, all from NBI. For the ASDEX case, flattop $P_{aux} \approx 8MW$, with 5MW from NBI and 3MW from ICRH to reduce central tungsten impurity concentration. Temporal evolution of the total plasma current, heating power, and confinement factor H_{98} for each pair can be seen in figure 1.

The vertical lines in the plots enclose the periods during which the kinetic profiles are averaged for analysis: 6.14-6.64s for JET 79626, 7.14-7.64 for JET 79630, and 5.25-5.75s for both ASDEX discharges. The periods differ for JET due to the different heating scheme timings. If the 79626 period were delayed, then the q-profile difference between the pair - the central point in this work - would be diminished in the analysis according to current diffusion modelling. While the decay in H_{98} in 79626 on the current diffusion timescale may seem indicative of the decay of the effect of the current overshoot on the q-profile, in fact the pedestal confinement of the two JET discharges do not remain the same at later times. The pedestal confinement in 79626 decays with time, contributing significantly to the observed reduction in H_{98}. This behaviour is not a regular feature of JET hybrids with current-overshoot at either low or high triangularity. For example, figure 1 in [9] illustrates improved confinement maintained throughout the flattop phase of a JET hybrid scenario discharge, over the current diffusion timescale. Full analysis

of the dynamics of the kinetic profiles is necessary to understand this maintenance of improved confinement following the application of current overshoot. This is however out of the scope of this work. We reiterate that the main purpose of this work is to isolate and validate the expected s/q impact on core confinement by comparing discharges in periods where they display similar pedestal confinement yet observed differences in both q-profile and core confinement. This is what is achieved by comparing the averaged kinetic profiles of the discharges within the abovementioned time windows.

All GLF23 analyses in this paper take background kinetic profiles and boundary conditions from the averaged periods defined above. Details of 0D quantities averaged over these periods can be found in table 8. Note that the AUG H_{98} factors quoted in the table are lower by 20% compared to the values quoted in [28] since here the energy content is calculated by integration of the kinetic profiles, as opposed to the AUG W_{mhd} diagnostic which includes the significant fast particle content. $< s/q >$ is defined as the volume averaged s/q between x=0.4-0.8, where x is the normalized toroidal flux coordinate. The average is carried out from x=0.4, since for $x < 0.4$ the magnetic shear is low ($s < 0.6$) and the short wavelength approximation within which equation 1 is derived may no longer hold. The averaging procedure is up to x=0.8, the approximate location of the GLF23 boundary conditions. All discharges are devoid of NTMs in the temporal periods studied, apart from AUG 20993, which has a 3/2 NTM in the vicinity of $x = 0.5$. The potential polluting effect of this mode on the isolation of the s/q impact on confinement for the AUG pair is examined in section 5.

The s/q and rotation profiles used throughout this analysis can be seen in figure 2, and the q-profiles themselves in figure 3. For the JET pair, the interpretative q-profiles were used since the transient effect of the current overshoot may in certain cases be within the error bars of the MSE measurements. By interpretative q-profiles, we mean q-profiles predicted by CRONOS through solving the current diffusion equation with prescribed temperatures and densities (from measurement), and calculated current drive sources. All interpretative simulations started early enough in the ramp-up phase such that the memory of the initial prescribed q-profiles were lost, and thus could not affect the eventual prediction. For the AUG pair, the measured q-profiles were used. This was because the interpretative q-profiles failed to reproduce the measured relaxed q-profiles within experimental error, as also seen in previous AUG improved H-mode modelling [29]. This may be due to MHD activity redistributing the current, clamping the q-profile to 1, as reported in [30, 31, 32]. While this may raise questions as to the validity of the JET interpretative q-profiles, previous CRONOS interpretative modelling of JET hybrid scenario current diffusion has shown agreement with experimentally measured q-profiles [9]. This increases the confidence in our choice in using the interpretive q-profiles for the JET discharges in this analysis.

Regarding q-profile measurement errors, the MSE measurement error for the AUG q-profiles are $\sim 10\%$. For the JET q-profiles, the modelled values are sensitive to the measured $< Z_{eff} >$, Z_{eff} profile shape, and bootstrap current calculations. A thorough assessment of the q-profile sensitivity to the modelling assumptions has not been carried

out for this work, apart from a Z_{eff} sensitivity check shown in section 4. However, both for the AUG and JET cases, the proximity of the shots (each pair was carried out in the same experimental session) means that it is likely that any systematic errors are the same for both discharges in each pair. Since we are concerned with *differences* in the q-profiles, this increases the reliability of the results. Nevertheless, it is indeed possible that the error in the difference between the q-profiles in each pair is of the order of the difference itself. This important caveat underlines this entire work.

The rotation profiles for the JET case are similar. For the AUG case, the 20993 (lower confinement) case has a significantly flatter rotation profile in the low magnetic shear region $x < 0.4$. It is possible that this flatter rotation profile is due to the magnetic braking induced by the 3/2 mode present in shot 20993.

A representative overview of the kinetic profile data and fit quality for all discharges analyzed in this paper can be seen in figure 4 *for single timeslices*. Spline fits were carried out for each timeslice. The fit polynomial order and break-points varied between the different profiles. JET T_i was measured by a combination of core and edge charge exchange (CXFM and CXSE) diagnostics. The CXSE is vital for determining the approximate equivalence of the T_i pedestal top values between the pair. However, the finite radial extension of the diagnostic does not allow the full resolution of the pedestal T_i profile. JET T_e was measured by both ECE and high resolution Thompson scattering (HRTS). The spline fit used both datasets on an equal footing. This is not ideal since the datasets are not fully mutually consistent. However, since the pedestal region (which will serve as the modelling boundary condition) is only resolved by HRTS, the choice of carrying out a combined data fit has no impact on the modelling results. Nevertheless, the lack of full agreement between the HRTS and ECE measurements should be maintained as a caveat when comparing the T_e modelling results to the fits from the experimental data. JET n_e was measured by HRTS.

For AUG, T_i was measured by CX. T_e was measured by ECE. n_e was measured by a combination of interferometry and lithium beam spectroscopy, and the data combined with the Integrated Data Analysis (IDA) approach [33].

For comparison of the kinetic profiles with the GLF23 predictions, the profiles were averaged for 0.5 s during the time windows displayed in figure 1. This is more than an energy confinement time for both machines. This averaging also significantly reduces the RMS error of the data points, to below 2% for example for both the JET and AUG T_i and V_{tor} measurements. The boundary conditions for the GLF23 simulations were also taken from this averaging. From this averaging we can also analyze R/L_{Ti}, to determine the location and robustness of the R/L_{Ti} differences between the shots of each pair. This can be seen in figure 5. These curves were made by time averaging the T_i spline fits made at each timeslice. The error from the scatter in these fits is 10% for the JET data, and 15% for the AUG data. We can see that the JET R/L_{Ti} differences are localized to the region x=0.6-0.8, while the AUG R/L_{Ti} differences are localized from x=0.25-0.7 (where x=0.25 is the approximate location of the innermost reliable T_i datapoint). While the error bars lead to overlap over much of the R/L_{Ti} profiles, the

errors are not independent. The scattering of one specific data point creates an opposing change in R/L_{Ti} on either side of the position of that point. This fact increases the robustness of the observed R/L_{Ti} differences and locations.

Finally, we compare the ratios of these experimental R/L_{Ti} profiles to the predicted analytical R/L_{Ti} ratios from equation 1. We note here that the R/L_n ratios of all discharges, particularly for $x > 0.5$, are low enough to satisfy the flat density profile approximation. The ratios are displayed in figure 6. We include analytical R/L_{Ti} ratios also assuming constant T_i/T_e, to separate the effect of s/q and T_i/T_e. Qualitatively the analytical and experimental ratios show the following similar features: in the JET case, the maximum observed difference for $x > 0.5$ is predicted by equation 1, with no predicted difference (as in the observations) in the region of x=0.4; for AUG, the increasing difference from 0.75 in towards the core is also predicted by equation 1. However, the observed difference in the AUG case for $x < 0.5$, the low magnetic shear region ($s < 0.6$), is not predicted. The T_i/T_e component has a minor influence on the predicted R/L_{Ti} differences, as can be seen by comparing the curves with and without constant T_i/T_e. The differences between the analytical and experimental ratios can be either due to additional physics setting the transport, beyond ITG linear threshold physics, and/or due to the errors in the q-profiles identified with each discharge. Nevertheless, the correlations which are observed are encouraging with regard to isolating s/q as a significant factor in the observed core confinement differences within each pair of discharges. These analytical results are corroborated by numerical predictions by both GLF23 and QuaLiKiz, as outlined in the following sections.

3. Modelling tools and techniques

The core of CRONOS is a 1.5D transport solver, whereby 1D current diffusion, particle and energy equations are solved up to the separatrix, self consistently with 2D magnetic equilibrium [22]. In this work, the NBI heat and current sources are calculated by NEMO/SPOT [34, 35]. The ICRH heat sources for the AUG discharges are calculated with PION [36]. The magnetic equilibrium is calculated with HELENA [37]. The neoclassical transport, bootstrap current, and neoclassical resistivity is calculated with NCLASS [38]. Turbulent transport is calculated with the GLF23 model [16, 23]. The fast particle profiles calculated by NEMO/SPOT and PION for NBI and ICRH are subtracted from the ion density profiles entered into GLF23. The calculated fast particle fractions for both the JET/AUG simulations successfully account for the observed differences in $\beta_N(W_{dia}/W_{mhd})$ and $\beta_N(W_{th})$.

For the JET simulations, GLF23 is employed within the region x=0-0.83, where x is the normalized toroidal flux coordinate. For the AUG simulations, GLF23 is employed within the region x=0-0.76, i.e. up to the outermost available CX measurement location. This minimizes the error due to the boundary condition uncertainty. The simulations are carried out on the energy confinement timescale, within the time periods displayed in figure 1, using background profiles and scalar quantities averaged in that period.

Both *heat transport only* simulations (with prescribed density profiles for measurement) and *combined heat and particle transport* simulations are carried out. As mentioned in section 2, the JET input q-profiles are taken from CRONOS interpretative runs (current diffusion only simulations), and the AUG q-profile inputs from MSE measurements. For each discharge, comparison simulations were carried out substituting the q-profile input with the q-profile from the other member of each pair. The magnetic shear is then recalculated by CRONOS in a self-consistent manner. In such a manner GLF23 predicts the confinement difference solely due to the changed values of the q-profile and magnetic shear. Further linear threshold analysis examining the effect of s/q is also carried out with the quasilinear gyrokinetic transport model QuaLiKiz [25].

4. Results: GLF23 q-profile substitution simulations

4.1. JET heat transport only

Figure 7 shows the T_i and T_e predictions for JET 79630. These simulations include *heat transport only*. Runs were carried out both with and without the GLF223 ExB turbulence suppression model, as specified by the α_{ExB} parameter. 79630 simulations with the substituted q-profile from 79626 (the improved confinement case) are also shown. The comparison of simulations with differing q-profile inputs is the central point of this work.

The inclusion of ExB suppression leads to overprediction of T_i. This overprediction is also seen in JETTO [39] simulations of the same discharge, verifying that this observation is not an artifact of the CRONOS/GLF23 methodology used in this work. However, independently of the degree of prescribed ExB suppression, the q-profile substitution leads to a degree of T_i increase comparable to the experimentally observed difference between the two discharges. A more quantitative analysis of these differences, and of all subsequent simulations discussed below, can be found in the tables in section 4.5. The slight differences between the JETTO and CRONOS simulations (for q79630) can be fully accounted for by the different smoothing techniques of the GLF23 output diffusivities employed in the codes. These smoothing technique induced differences have been verified to be systematic, and do not affect the predicted relative differences when substituting the q-profile.

4.2. AUG heat transport only

This pattern is replicated in the AUG simulations, displayed in figure 8 for a heat transport simulation of shot 20995. In the AUG 20993 case the degree of T_i overprediction is more severe. However, regardless of the ExB suppression assumption, the q-profile substitution leads to a T_i difference qualitatively consistent with experimental observations.

4.3. JET combined heat and particle transport

In figure 9, the results of *combined heat and particle transport* simulations for JET 79630 are shown. The pattern remains similar to the heat transport only cases, although the primary effect of confinement improvement following the q-profile substitution is now in the particle channel. Compared to the heat transport only case, the T_i profile increase is reduced when switching to the 79626 q-profile. This is due to the increased transport predicted by GLF23 due to the increased density gradients, interpreted as the destabilization of TEM modes due to the propagation of the mode in the electron diamagnetic direction.

4.4. AUG combined heat and particle transport

The AUG heat and particle transport simulations show similar results to the JET heat and particle transport case. The AUG 20995 simulations are displayed in figure 10. For the AUG case, the degree of improved particle transport is consistent with observation, although when ExB suppression is included the n_e profiles are significantly higher than the measured values.

4.5. Summary of GLF23 runs

In tables 2 and 3, the simulation results are summarized in terms of the predicted core thermal energy content: $W_{core} = \frac{3}{2}\int_0^{x_{bc}}(P_{th}(x) - P_{th}(x_{bc}))Jdx$. P_{th} is the thermal pressure. x_{bc} is taken at the GLF23 operational zone boundary at x=0.83/0.76 for JET/AUG. J is the Jacobian corresponding to the volume element. The tables summarize - according to GLF23 - the extent of the s/q effect *alone* in explaining the core confinement *differences* between each pair, both including and excluding ExB shear stabilization.

In spite of the absolute core energy content overprediction when including ExB shear stabilization, the degree of change when substituting the q-profile is maintained both with and without ExB shear stabilization. The degree of change also remains the same when including particle transport, due to the aforementioned increase in heat transport when increasing the density gradients. Taking the average of the GLF23 simulated core energy content for all runs, we obtain a ratio for 1.105 for the JET runs, and 1.17 for the AUG runs. This corresponds to the s/q effect *alone* contributing to 60% of the core confinement difference for the JET pair, and 35% of the core confinement difference in the AUG pair, according to GLF23. In section 5 we discuss other possible contributions to the core energy content differences.

4.6. Sensitivity of JET results to choice of Z_{eff} and α_{ExB}

The Z_{eff} taken for the JET simulations had an assumed form of $Z_{eff} \propto n_e^{-0.4}$, and was normalized such that the line average $< Z_{eff} >$ agrees with Bremsstrahlung measurements. However, as seen in figure 11, this assumption does not agree

with Z_{eff} profiles calculated from carbon concentration measurements carried out by recombination charge exchange spectroscopy (CX). For $x > 0.8$, where no CX measurements were available, an assumed near constant CX Z_{eff} profile was prescribed.

The sensitivity of the calculated q-profile to Z_{eff} was examined by repeating the interpretative run for 79630 with alternative Z_{eff} profiles based on the discrepancy between the Bremsstrahlung and CX measurements. Since the CX measurements were only available following application of the neutral beam injection, neither precise information on the Z_{eff} profile shape in the early phase of the discharge, nor an alternative value of $< Z_{eff} >$ was available. Therefore, we tested the sensitivity by simply assuming a Z_{eff} profile identical to the CX profile from figure 11, and reducing $< Z_{eff} >$ in the interpretative run by a constant factor ~ 1.3, typical of the discrepancy between the Bremsstrahlung and CX measurements.

The impact of using the CX Z_{eff} profile in the GLF23 simulations was also examined. Both the 79630 heat transport only and combined heat and particle transport simulations were repeated using CX Z_{eff} profiles averaged over the 7.14-7.64s time window. Finally, the same simulations were repeated when reducing the GLF23 α_{ExB} parameter to 1. The heat transport only results are seen in figure 12, and the combined heat and particle transport results in figure 13.

The q-profile sensitivity to the Z_{eff} profile, within the range studied, is small. However, the variation of the T_i predictions when switching to the CX measured Z_{eff} profile is not negligible, and is primarily due to reduced dilution. When combined with switching to $\alpha_{ExB} = 1$, the ion temperature overprediction, while still apparent, is significantly diminished. This more minor level of T_i overprediction is consistent with GLF23 results reported in [40], where both CX Z_{eff} profiles and $\alpha_{ExB} = 1$ were employed. Also in the combined heat and particle transport case, the degree of averaged n_e overprediction is reduced when switching to the CX Z_{eff} profile, although the profile peaking still remains well above the experimentally observed value. We reiterate that the relative differences due to the s/q effect - the central point of this work - are invariant to the choice of Z_{eff} and α_{ExB}.

5. Additional contributions to core confinement differences

In this section we explore possibilities - other than the s/q effect - for explaining the observed differences in core confinement for both the JET and AUG pairs.

5.1. Density profiles

For the heat transport only simulations, the prescribed density profile may have an effect on the predicted core confinement. This may be due to both the inherent different stored energy content, and also the R/L_n parameterization of the predicted transport. In figure 14 a comparison of AUG 20995 heat transport simulations prescribing both the 20995 and 20993 density profiles is displayed. This sensitivity test was carried out

for AUG since the $\overline{n}$ difference for the AUG pair is greater than the JET pair: 6% as opposed to 3%.

The resulting difference in W_{core} is a negligible $< 1\%$ increase when prescribing the 20993 n_e profile as opposed to the 20995 profile, for the no ExB suppression case. The increase in $T_{i,e}$ compensates for the decreased $n_{e,i}$ profiles. For the full ExB suppression case, prescribing the 20993 n_e profile led to a 6% *decrease* in W_{core}. The discrepancy between the two cases can be traced to the flat temperature profiles in the 20995 n_e case located at $x = 0.4$. This is an artifact of GLF23 modelling, where typically above a certain R/L_n threshold the sensitivity of the transport to R/L_n increases greatly. Evidently the 20995 R/L_n is at that threshold around $x = 0.4$. However, these TEM modes, which leads to a flat temperature profile in the region of $x = 0.4$ in the $\alpha_{ExB} = 0$ case, are stabilized by the ExB suppression model when $\alpha_{ExB} = 1.35$. Thus the flat temperature profile in the $x = 0.4$ region in the $\alpha_{ExB} = 0$ case is not evident in the $\alpha_{ExB} = 1.35$ case.

5.2. Z_{eff}

Sensitivity of the transport to Z_{eff} is examined for the JET pair, which displays a greater difference in measured $< Z_{eff} >$ compared to the AUG case: 12% as opposed to 3%. The improved confinement discharge has lower $< Z_{eff} >$ in both pairs. In figure 15 two separate JET 79630 simulations are compared, with the differing Z_{eff} profiles. The simulations include both particle and heat transport, and no ExB suppression is included in these simulations. The results show that the sensitivity is small but not entirely negligible: the 79626 Z_{eff} case has an increased W_{core} by 4% compared to the 79630 Z_{eff} case, which is also in the correct direction of the experimentally observed improvement.

5.3. Heat and particle sources

Simulations which compare the effect of substituting only the heat and particle source profiles were carried out, to test the sensitivity of the predicted core energy content on the precise source profiles. However, due to the highly stiff nature of the GLF23 model, the predicted changes in W_{core} following such substitutions were completely negligible ($< 1\%$).

5.4. GLF23 boundary conditions

The largest part of the observed difference in confinement between each pair of discharges is from the core. However, the differences in the values of the kinetic profiles at the GLF23 boundary conditions - x=0.83 for the JET pair and x=0.76 for the AUG pair - can still play a significant role. To test the impact of the boundary condition on the core confinement, we first note that from the definition of the gradient length $1/L_T = \frac{dT/dr}{T}$, we can obtain $T(r) = T(r_{bc})exp(\int_{r_{bc}}^{r} 1/L_T(r)dr)$, where we have taken a temperature

gradient length for this example, and r_{bc} is the boundary condition radius. If we then assume that the inverse gradient lengths of the kinetic profiles would be maintained following slight changes in the boundary condition values, then the modification of the kinetic profiles following a change in the boundary conditions can be calculated by a simple multiplication of each profile corresponding to the change in each respective boundary condition value. In such a case, the effect of these boundary conditions on the core confinement can be easily examined. We can recalculate the experimental W_{core} by simply multiplying the experimental kinetic profiles by factors corresponding to the ratios of the boundary conditions between the discharges in each pair. This assumption was tested with GLF23 simulations, and was found to be adequate.

The 79630 experimental kinetic profiles were multiplied to match the 79626 boundary conditions, and W_{core} recalculated. The recalculated W_{core} was 5% higher than the original W_{core}. Thus, the boundary conditions alone may be responsible for $\sim 30\%$ of the perceived core confinement difference. For the AUG case, setting the 20993 experimental kinetic profiles to the 20995 boundary conditions showed that $\sim 20\%$ of the perceived core confinement difference may be due to the boundary conditions.

Note that while the boundary condition values may be related to the height of the ETB (pedestal), the correlation is not direct since the boundary condition locations for the GLF23 modelling do not coincide with the pedestal top. Particularly for the AUG simulations, the boundary condition is limited by the outermost data point of the T_i diagnostic, and no data on the actual T_i pedestal height is available.

5.5. NTM effect

While the pair of JET discharges do not have any NTMs within the temporal period of analysis, AUG 20993 (the lowered confinement case) has a low amplitude 3/2 NTM located in the vicinity of $x = 0.5$. While it is difficult to precisely measure the impact of this NTM on confinement, we estimate the maximum possible impact of NTM by comparing the experimental T_e (figure 16), normalized to the same boundary condition at $x = 0.76$. The T_e differences are indeed localized to the region $x < 0.5$, in line with a possible relation to the NTM activity. The ratio between the profiles is also seen in figure 16. For this estimation, we make a strong assumption that these T_e differences are fully due to the NTM, and not due to the differing q-profile and rotation profiles. We can then assess the potential impact of the NTM by multiplying all kinetic profiles ($T_{i,e}$, $n_{i,e}$) of discharge 20993 by this ratio for $x < 0.5$, and recalculate W_{core}. This led to a W_{core} increase of 20993 of 17% of the total difference between 20993 and 20995. We can thus conclude that while the NTM may have a non-negligible impact on core confinement, the impact is not large enough to fully explain the remaining 40% difference in W_{core} for the AUG pair following taking into account the s/q effect and the boundary condition effect.

5.6. Predictions in the low magnetic shear region

In figure 17 we compare the predicted R/L_{Ti} profiles from the GLF23 simulations with the observed values, for both pairs of discharges. The results shown are from simulations including heat transport only, and the results both with and without ExB suppression are shown. The absolute predictions - particularly when including ExB suppression - deviate from the observations. However, the relative predictions - when substituting the q-profile - agree with the observations.

In the JET case, the location of the R/L_{Ti} differences when substituting the q-profile agrees with the location of the s/q differences, as seen in figure 2. The location of these differences also fully agrees with the observations. For the AUG pair, this is also the case for $x > 0.4$, but the observed differences in R/L_{Ti} within the region $x < 0.4$ are not predicted by GLF23. This region corresponds to the low magnetic shear region ($s < 0.6$). Note that in the $\alpha_{ExB} = 0$ AUG case, the dip of R/L_{Ti} at around $x = 0.4$ is due to the density gradient exceeding a threshold beyond which transport is greatly increased in GLF23. When replacing the density profiles with the 20993 profiles, this dip is not seen, but the relative differences in R/L_{Ti} when substituting the q-profile are maintained. When including ExB shear in the AUG case, the predicted R/L_{Ti} differences slightly increase in the $x = 0.4$ region. This is due to the difference in rotation profiles, also seen in figure 2. However, this is still insufficient to explain the observed R/L_{Ti} differences for $x < 0.4$, which contributes to the observed W_{core} difference between AUG 20993/20995. A further proportion of the W_{core} difference in the AUG pair thus comes from the low magnetic shear region, a difference which is not predicted by GLF23.

6. QuaLiKiz linear threshold analysis

Additional analysis was carried out for both the JET and AUG cases with QuaLiKiz, where we assess the sensitivity of the instability linear thresholds to the q-profile, at the locations $x = 0.35, 0.45, 0.55, 0.65, 0.75$. This was carried out by a QuaLiKiz R/L_{Ti} scan, to identify the linear threshold. The QuaLiKiz calculations took as input the parameters for 79630 for the JET pair, and 20995 for the AUG pair. The simulation at each radial point was then repeated after replacing q and s with the values from 79626 and 20993 respectively. The results are seen in figure 18. The QuaLiKiz results are compared to the experimental R/L_{Ti} calculated in two ways: with respect to a radial coordinate defined as $(R_{in} - R_{out})/2$, where $R_{in,out}$ are the radii to the high field and low field side flux surfaces on the midplane; with respect to the radial coordinate defined as R_{out}. R/L_{Te} was kept at the observed ratio to R/L_{Ti} throughout the QuaLiKiz R/L_T scans.

The differences in predicted R/L_{Ti}, compared to the observed values, is recovered well by QuaLiKiz purely when replacing the input q and s values. This corroborates the GLF23 predictions. For JET, the radial positions of the predicted R/L_{Ti} difference

matches the observed positions: no difference for $x < 0.5$ and an increasing difference for $x > 0.5$. For AUG, the location of the differing R/L_{Ti} predictions fits the observations for $x > 0.5$, with almost no difference in the vicinity of the boundary condition at $x = 0.77$, and an increasing difference towards midradius. For $x < 0.5$, the predicted differences are less than the observed differences, but the discrepancy is less than in the GLF23 case. We note here that at the radial position x=0.35 in AUG the precise predictions are highly sensitive to the precise value of measured magnetic shear. This is due to the $s - \alpha$ geometry model employed in QuaLiKiz leading to α-stabilization at low levels of magnetic shear. For $(s - \alpha) < 0$, the modes are stabilized. Thus the lower magnetic shear for the 20995 case (0.28 vs 0.35) at similar levels of α_{MHD} (~ 0.35) leads to higher thresholds. When carrying out the simulations with prescribed $\alpha_{MHD} = 0$, the predicted R/L_{Ti} thresholds at x=0.35 differ by only 5% between the 20995 and 20993 cases.

In comparison with the $R = (R_{in} + R_{out})/2$ defined gradients, the QuaLiKiz results also overpredict R/L_{Ti} for $x > 0.5$ - the high magnetic shear region. However, if we compare the predictions to the gradients defined by $R = R_{out}$, the agreement is much approved for $x > 0.5$. At high magnetic shear - characteristic of hybrid scenarios - the ITG modes are more strongly ballooned to the low field side due to the increased ion Landau damping. We speculate here that in such situations, it may be more appropriate to input experimental gradients defined with $R = R_{out}$ into the model. This topic, as well as profile stiffness at low magnetic shear, is currently under investigation as part of the ongoing development of the QuaLiKiz transport model.

7. Discussion and conclusions

7.1. GLF23 results

For both JET 79630 and AUG 20995, the absolute W_{core} values are significantly overpredicted when including ExB shear suppression in the GLF23 model. Without ExB shear suppression, W_{core} is well predicted in both the heat transport only and combined heat and particle transport simulations. It is difficult to determine whether this overprediction is due to a deficiency in the ExB suppression model, or due to an intrinsic overprediction of the underlying instability thresholds. We note that GLF23 simulations for high triangularity JET hybrids also display a similar T_i overprediction as seen in this present work [41]. However, in previous work, the JET hybrid discharge 58323 was shown to be satisfactorally predicted by GLF23 [42], even when including ExB suppression. A simulation of this discharge was repeated with the same CRONOS/GLF23 methodology performed in this work, and the previous result was indeed recovered. However, additional simulations taking into account the uncertainties in Z_{eff}, combined with the resultant differences in the modelled q-profile, also led to T_i overpredictions as seen here. For other JET discharges analyzed in [42], numerous examples of significant T_i deviations can be seen in figure 4. Also in this work, the

degree of overprediction - while still significant - is reduced when using the Z_{eff} profile from charge-exchange measurements as shown in section 4.6.

These results highlight the modelling sensitivity to the input parameters, which helps explain the scatter in the literature with regard to the degree of predicted GLF23 T_i overprediction. We also note that in recent TGLF [43] modelling of DIII-D hybrid discharges [44], T_i was reported to be significantly underpredicted when not employing ExB suppression. However, the ion energy transport was reported to be reduced to neoclassical levels, while the neoclassical transport was taken from a modified Chang-Hinton model. This model yields diffusivities larger than that calculated by first-principle methods such as by the NCLASS [38] model employed in this work. This may lead to more pessimistic T_i predictions. Further validation of the various transport models on discharges from different machines, while employing using the same modelling methodology to reduce scatter induced by different modelling assumptions, would be highly beneficial.

Another potential source of discrepancy between the model and the experiment is the flux surface geometry. GLF23 assumes shifted circle geometry in the large aspect ratio limit. However, shaping and finite aspect ratio can be quite important in setting the linear thresholds. An extensive study of ETG linear thresholds from linear gyrokinetic calculations, including shaping, was carried out in [45]. The study assumed adiabatic ions. The obtained (from fitting) ETG linear threshold formula is thus isomorphic to the ITG case assuming adabatic electrons, which we rewrite as follows:

$$\left(R/L_{Ti}\right)_c = max\left\{(1+T_i/T_e)(1.33+1.91\frac{s}{q}q)(1-1.5\epsilon)\times[1+0.3\epsilon(d\kappa/d\epsilon)], 0.8R/L_n\right\} \quad (3)$$

where $\epsilon = r/R$ and κ is the elongation. Equation 3 is very similar to equation 1 apart from the increased weight of s/q, and the geometrical terms. These terms are of more importance at higher radii, and specifically for JET 79630 at $x = 0.65$, $(1-1.5\epsilon)(1+0.3\epsilon(d\kappa/d\epsilon)) \sim 0.8$, which would reduce the modelled R/L_{Ti}. This is consistent with the observation that even with no ExB shear included ($\alpha_{ExB} = 0$), the GLF23 model overpredicts R/L_{Ti} for $x > 0.5$ as seen in figure 17.

With regard to potential explanations for a deficiency in the GLF23 ExB suppression model, we note that discharges considered here are highly NBI-driven discharges, with a relatively high degree of rotational shear. It has been shown that due to parallel velocity shear the efficiency of ExB shear in decreasing transport decreases at high rotation [46, 47, 48]. This may be relevant also for the increased q_{95} hybrid discharges. At higher q, the parallel (to the field line) component of the toroidal velocity is increased. While parallel velocity shear destabilization is included in GLF23, the destabilization effect is minor for the rotation velocities considered here. This is seen in figure 19 where we compare JET 79630 GLF23 T_i predictions (with heat transport only), for cases where the ExB suppression model is not included ($\alpha_{ExB} = 0$), and where the toroidal velocity itself is set to zero ($V_{tor} = 0$). The difference between the predictions corresponds to the parallel velocity shear destabilization, which in this case only reduces the T_i profile by $\sim 2\%$.

Recent results at JET show that the effect of rotational shear in increasing R/L_{Ti}

(due to decreased stiffness) is located only in the low magnetic shear region, in our case $x < 0.4$ [14, 15]. However, this is inconsistent with the main effect of including GLF23 ExB suppression in our simulations, which increases R/L_{Ti} primarily in the high magnetic shear region $x > 0.5$. Additionally, other recent JET results show that R/L_{Ti} in $x > 0.5$ does not vary with the NB/IC heating mix, at constant total power, even if the rotation profiles varies significantly [49]. This is corroborated by previous analysis of an AUG improved H-mode discharge [29], where core R/L_{Ti} was not observed to increase following a significant increase of NBI power during the discharge, which led to increased rotation. Furthermore, analysis of the same discharge with the Weiland model [50] predicted no significant improvement in core confinement due to rotation.

The question of how to model and predict the effect of rotation on transport is thus still an open one. Nevertheless, the central point of this work is to verify the *relative* effect of the q-profile in leading to the difference in W_{core} between the two shots within each pair. This was examined with GLF23 simulations substituting the q-profile - the 79626 q-profile into 79630 simulations, and the 20993 q-profile into 20995 simulations. The results are discussed below.

7.1.1. JET 79630/79626 q-profile substitution A significant proportion of improved confinement in the JET hybrid scenarios analysed here is due to an increase in the ITG threshold due to improved q-profile shaping in the high magnetic shear region, at $x > 0.4$, according to GLF23. A proportion of $\sim 60\%$ of the observed improvement in core is predicted through q-profile substitution alone. In the heat transport simulations, differences in R/L_{Ti} are in the JET case only observed in the high magnetic shear region ($x > 0.4$) and are correlated with differences in s/q. This relative difference in W_{core} is independent of the inclusion of the ExB suppression model in GLF23. In the combined heat and particle simulations, the primary channel of confinement improvement is n_e.

The majority of the remaining 40% of core confinement difference can be linked to the differences in GLF23 boundary conditions at x=0.83. A further $\sim 30\%$ of the difference can be attributed to the boundary conditions. Slight differences in n_e and Z_{eff} between the shots can account for the remaining proportion.

7.1.2. AUG 20995/20993 q-profile substitution Approximately $\sim 55\%$ of the observed W_{core} difference can be accounted for by a combination of the s/q effect (35%) and the difference in boundary conditions ($\sim 20\%$). Again, this is independent of the ExB suppression model. It has been estimated that the NTM in 20933 may be responsible for up to a further $\sim 20\%$ of the difference. As in the JET case, the improvement due to the s/q effect is predicted to be primarily in the particle channel when including particle transport in GLF23.

The observed R/L_{Ti} differences occur both in the low and high magnetic shear regions within x=0.2-0.6. The R/L_{Ti} difference in the high shear region is correlated with a difference in s/q. However, the difference in the low shear region cannot be explained by s/q effects, according to GLF23. Due to the difference in rotational shear

for $x < 0.4$ between the two discharges in the AUG case (see figure 2), it may be possible that reduced stiffness in the low shear region (not predicted by the stiff GLF23) may account for a further proportion of core confinement difference, as also observed in JET [14, 15]. It is possible that the low amplitude NTM present in 20993 at around x=0.5 is responsible for a slight local difference in observed R/L_{Ti} in the x=0.5 region. However, the NTM cannot explain the observed differences in R/L_{Ti} for $x < 0.4$.

7.2. Final conclusions

The *differences* in W_{core} between the JET discharges can be fully accounted for: mostly by the s/q impact on ITG linear thresholds (60%) with an additional contribution from the boundary conditions, n_e, and Z_{eff}. The majority of the total W_{core} difference in the AUG pair can also be accounted for, although only 35% from the s/q effect alone. The potential importance of the differing rotation profiles within $x < 0.5$ (low magnetic shear zone) on the observed R/L_{Ti} profiles in that region is still an open question, and could explain the remaining W_{core} difference unaccounted for. The overprediction of W_{core} in GLF23 when including the full ExB suppression model also opens up questions regarding: accuracy of Z_{eff} for modelling input, accuracy of the parallel velocity shear destabilization model, the mechanism of ExB shear suppression (threshold shift vs stiffness reduction), the definition of experimental gradients at high magnetic shear for modelling input, and the role of finite aspect ratio and elongation. Nevertheless, the W_{core} *differences* can be satisfactorally predicted regardless of the ExB model, and the s/q profile plays a significant role in these predictions. These GLF23 predictions are also corroborated by R/L_{Ti} threshold analysis using QuaLiKiz. A general caveat is that the relatively low magnitude of the experimentally observed and calculated differences in both R/L_{Ti} and the q-profile demands that these conclusions be treated with caution. The small magnitude of the effect - a H_{98} increase of up to ~ 0.1 due to s/q only - hinders the experimental isolation of the s/q impact which can be in general be easily masked by competing effects and experimental error. Nevertheless, the results obtained here are consistent with the theoretically expected impact of q-profile shaping on core-confinement through threshold increase at outer radii and provides an encouraging validation in this regard. In ITER operational scenario studies, such H_{98} improvements of up to ~ 0.1 due to q-profile shaping have in fact been shown to have a significant impact on the projected fusion power in the ITER hybrid scenario [26]. Validation of these ITER predictions made with GLF23 was the inital driving motivation for this work. Further q-profile shaping experiments aiming for larger differences would be extremely helpful for continued study of the q-profile impact on transport.

ACKNOWLEDGEMENTS

This work, supported by the European Communities under the contract of Association between EURATOM/FOM and EURATOM/CEA, was carried out within the Predictive analysis of q-profile influence on transport in JET and AUG hybrid scenarios18 framework of the European Fusion Programme with financial support from NWO. The views and opinions expressed herein do not necessarily reflect those of the European Commission. This work is supported by NWO-RFBR Centre-of-Excellence on Fusion Physics and Technology (Grant nr. 047.018.002). The authors are grateful to W. Goedheer, G. Sips, I. Voitsekhovitch, and E. Westerhof for fruitful discussions.

REFERENCES

[1]. Gormezano C. et al Progress in the ITER Physics Basis Chapter 6: Steady state operation 2007 Nuclear Fusion **47** S285.
[2]. Luce T.C. et al 2003 Nuclear Fusion Nuclear Fusion **321**.
[3]. Sips A.C.C. et al 2002 Plasma Physics and Controlled Fusion **44** B69.
[4]. Joffrin E. et al 2005 Nuclear Fusion **45** 626.
[5]. Isayama A. et al 2003 Nuclear Fusion **43** 1272.
[6]. ITER Physics Expert Group on Confinement et al ITER Physics Basis Chapter 2: Plasma confinement and transport 1999 Nuclear Fusion **39** 2175.
[7]. Wade M.R. et al 2005 Nuclear Fusion **45** 407.
[8]. Sips A.C.C. et al 2007 Nuclear Fusion **47** 1485.
[9]. Joffrin E. et al in Fusion Energy 2010 (Proc. 23rd Int. Conf. Daejeon, 2010) (Vienna: IAEA).
[10]. Maggi C.F. et al 2007 Nuclear Fusion **47** 535.
[11]. Maggi C.F. et al 2010, Nuclear Fusion **50** 025023.
[12]. McDonald D.C. et al 2008 Plasma Physics and Controlled Fusio **50** 124013.
[13]. Politzer P.A. et al 2008 Nuclear Fusion **48** 075001.
[14]. Mantica P. et al 2011 Physical Review Letters **107** 135004.
[15]. Mantica P. et al 2011 Plasma Physics and Controlled Fusion **53** 124033.
[16]. Waltz R.E. et al 1997 Physics of Plasmas **7** 2482.
[17]. Guo S.C. and Romanelli F. 1993 Physics of Fluids B **5** 520.
[18]. Bourdelle. C et al 2002 Nuclear Fusion **42** 892-902.
[19]. Fourment C. et al 2003 Plasma Physics and Controlled Fusion **45** 233.
[20]. Hoang G.T. et al 2003 Physics of Plasmas **10** 2 405.
[21]. Hoang G.T. et al 2001 Physical Review Letters **12** 87 125001.
[22]. Artaud J.F. et al 2010 Nuclear Fusion **50** 043001.
[23]. Kinsey J.E. et al 2005 Physics of Plasmas **12** 052503.
[24]. Petty C.C. et al Physics of Plasmas **11** 3.
[25]. Bourdelle. C et al 2007 Physics of Plasmas **47** 14 112501.

[26]. Citrin J. et al 2010 Nuclear Fusion **50** 115007.
[27]. Hobirk J. et al submitted to Plasma Physics and Controlled Fusion.
[28]. Stober J. et al 2007 Nuclear Fusion **47** 728.
[29]. Na Yong-Su et al 2006 Nuclear Fusion **46** 232.
[30]. Gunter S. et al 1999 Nuclear Fusion **39** 1535.
[31]. Casper T.A. et al 2007 Nuclear Fusion **47** 825.
[32]. Petty C.C. et al 2009 Physical Review Letters **102** 045005.
[33]. Fischer R. et al 2010 Fusion Science Technology **58** 675-84.
[34]. Schneider M. et al 2009 Nuclear Fusion **49** 7 125005.
[35]. Schneider M. et al 2011 Nuclear Fusionn **51** 063019.
[36]. Eriksson L.-G. et al 1993 Nuclear Fusion **33** 1037.
[37]. Huysmans G.T.A. et al 1991 CP90 Conf. on Comp. Physics (Singapore: Word Scientific) p 371.
[38]. Houlberg W.A. et al 1997 Physics of Plasmas **4** 3230.
[39]. Cenacchih G. et al ENEA RT/TIB/88/5 (1988).
[40]. Voitsekhovitch I. et al 2009 Nuclear Fusion **49** 055026.
[41]. Joffrin E. et al 2010 EPS Conf. on Plasma Phys. (Dublin) P1.1047, http://ocs.ciemat.es/EPS2010PAP/pdf/P1.1047.pdf.
[42]. Kinsey J.E. et al 2005 Nuclear Fusion **45** 250.
[43]. Kinsey J.E. et al 2008 Nuclear Fusion **15** 055908.
[44]. Kinsey J.E. et al 2010 Physics of Plasmas **17** 122315.
[45]. Jenko F. et al 2001 Physics of Plasmas **8** 4096.
[46]. Kinsey J.E. et al 2005 Physics of Plasmas **12** 062302.
[47]. Highcock E.G. et al 2010 Physical Review Letters **105** 215003.
[48]. Barnes M. et al 2010 Physical Review Letters **106** 175004.
[49]. Versloot T.W. et al 2011 Nuclear Fusion **51** 103033.
[50]. Weiland J. et al 1989 Nuclear Fusionn **29** 1810.

Table 1. 0D quantities for all discharges analysed in this paper. Quantities averaged over 7.14-7.64s and 6.14-6.64s for JET 79630 and 79626 respectively, and 5.25-5.75s for AUG 20993 and 20995 .

Shot	B_T [T]	I_p [MA]	β_N (W_{th})	β_N (W_{dia}/W_{mhd})	$< s/q >$	Z_{eff}	H_{98}	MHD activity
JET 79630	2	1.7	1.9	2.6	0.79	1.97	1.13	3/2 NTM from 7.7 s
JET 79626	2	1.7	2.1	2.8	0.94	1.76	1.26	No appreciable activity
AUG 20993	2.4	1	1.6	1.9	0.69	2.42	0.98	Weak 3/2 NTM
AUG 20995	2.4	1	1.9	2.3	0.84	2.35	1.2	Fishbones

Table 2. Core thermal energy following GLF23 predictions for JET hybrids. Units are [MJ].

	EXP	Heat transport		Heat and particle	
		no ExB	with ExB	no ExB	with ExB
79630 (q30)	1.67	1.71	2.37	1.71	2.68
79630 (q26)	1.97	1.9	2.62	1.83	3.03
Ratio	1.17	1.11	1.11	1.07	1.13

Table 3. Core thermal energy following GLF23 predictions for AUG hybrids. Units are [MJ].

	EXP	Heat transport		Heat and particle	
		no ExB	with ExB	no ExB	with ExB
20995 (q93)	0.2	0.249	0.367	0.255	0.371
20995 (q95)	0.294	0.293	0.421	0.3	0.429
Ratio	1.47	1.18	1.15	1.18	1.16

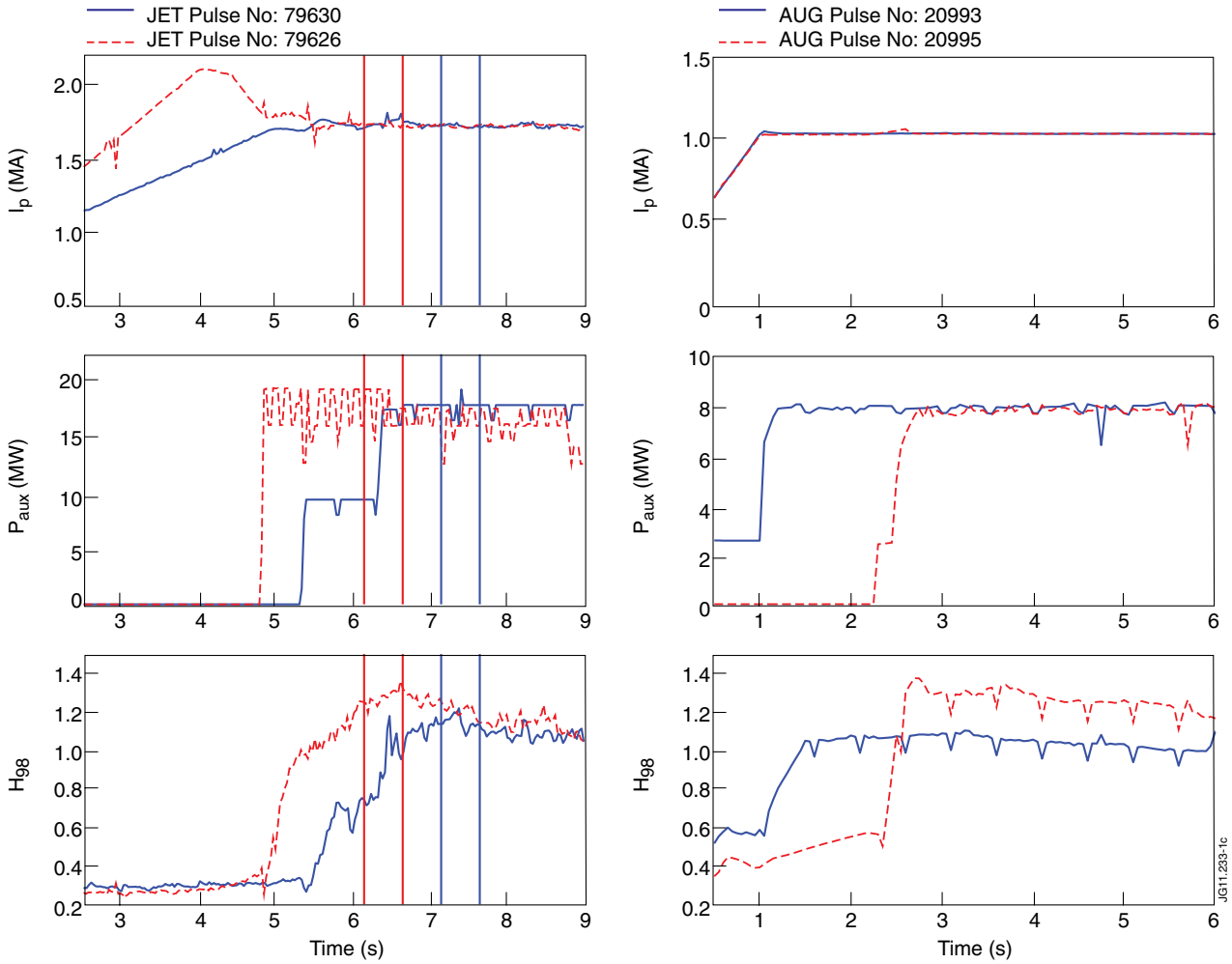

Figure 1: Temporal evolution of total plasma current (upper row), total auxilliary heating power $P_{aux} = P_{NBI} + P_{ICRH}$ (center row), and H98 confinement factor (lower row) for the JET pair 79626/79630 (left panels) and AUG pair 20993/20995 (right panels).

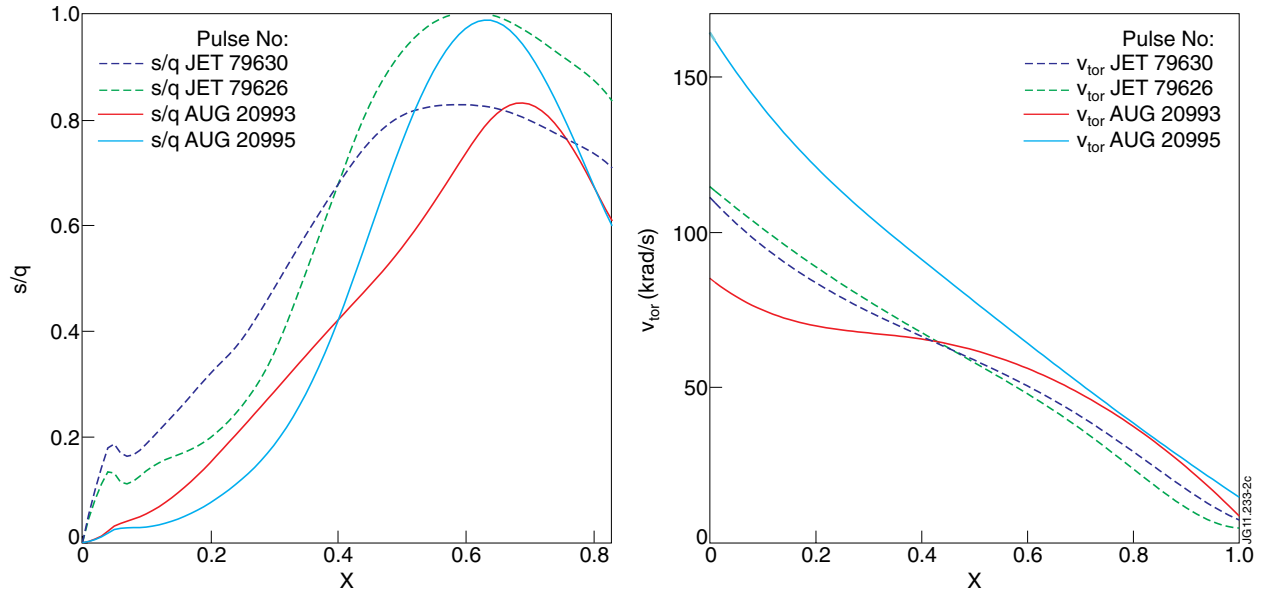

Figure 2: s/q profiles (left panel) and toroidal rotation profiles (right panel) for all discharges analysed in this paper.

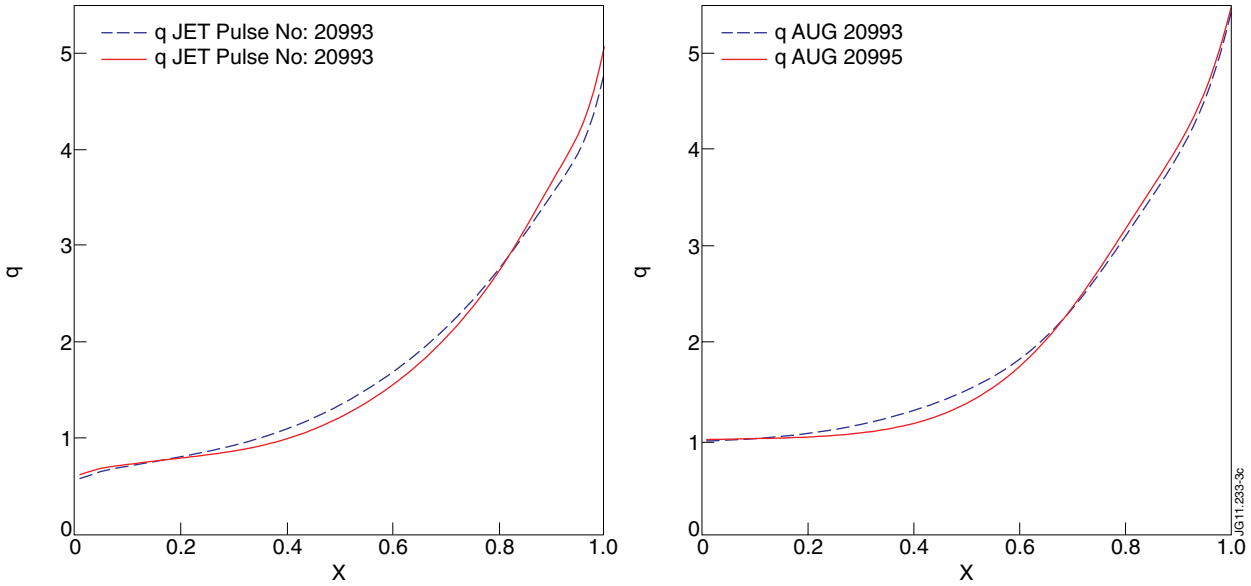

Figure 3: q-profiles used for the analysis of the JET discharges (left panel) and for the AUG discharges (right panel).

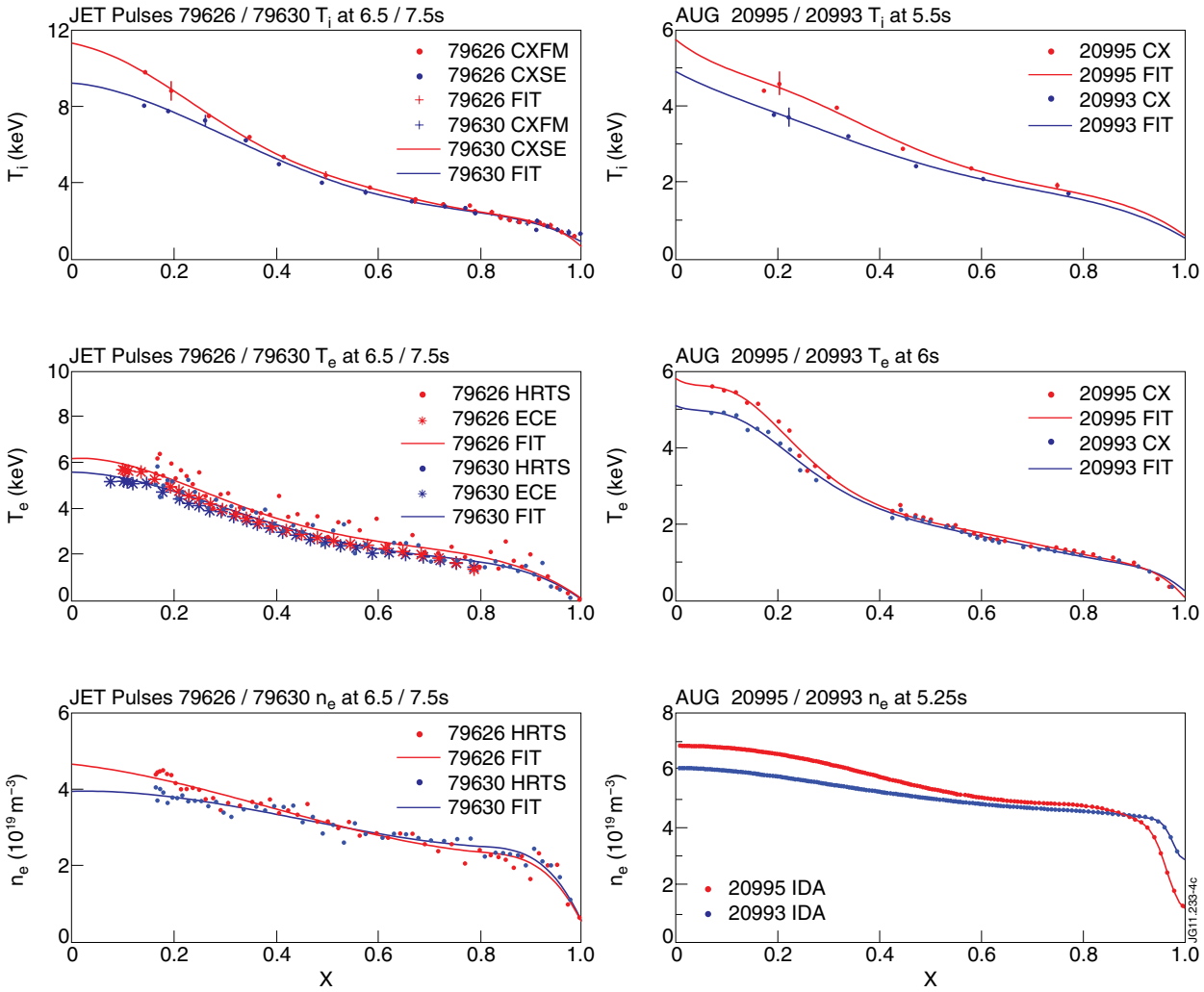

Figure 4. T_i (top row), T_e (center row) and n_e (bottom row) profiles for JET Pulse No's: 79626/30 (left panels) and AUG 20993/95 (right panels).

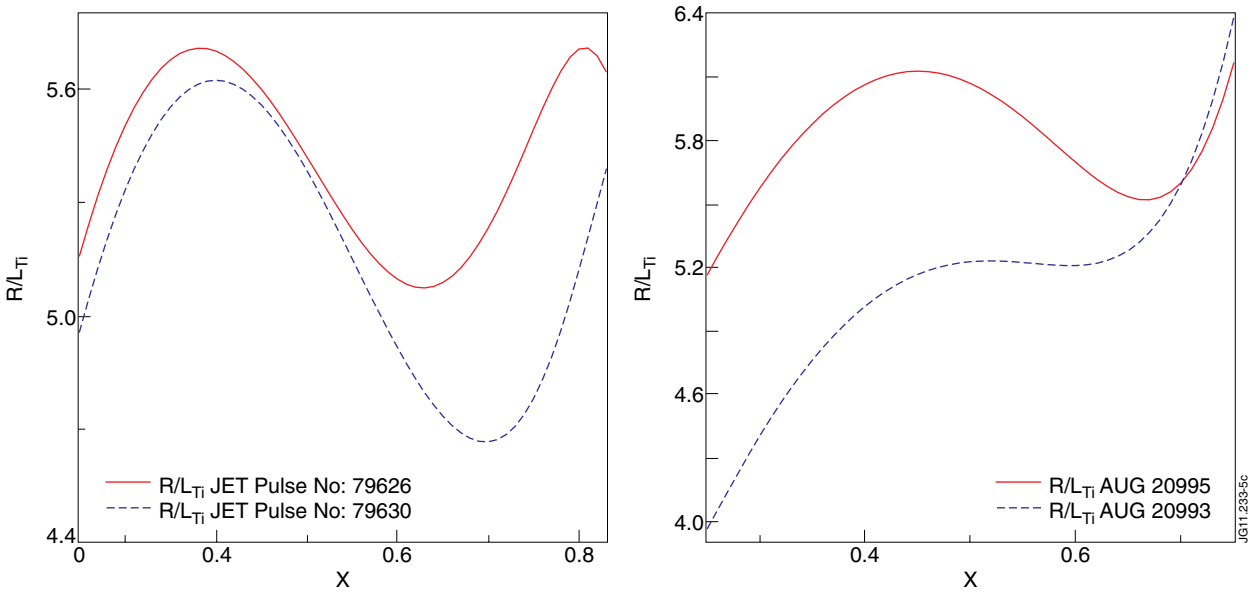

Figure 5: R/L_{Ti} profiles for JET Pulse No's: 79626/30 (left panel) and AUG 20993/95 (right panel), for T_i profiles averaged over 0.5s.

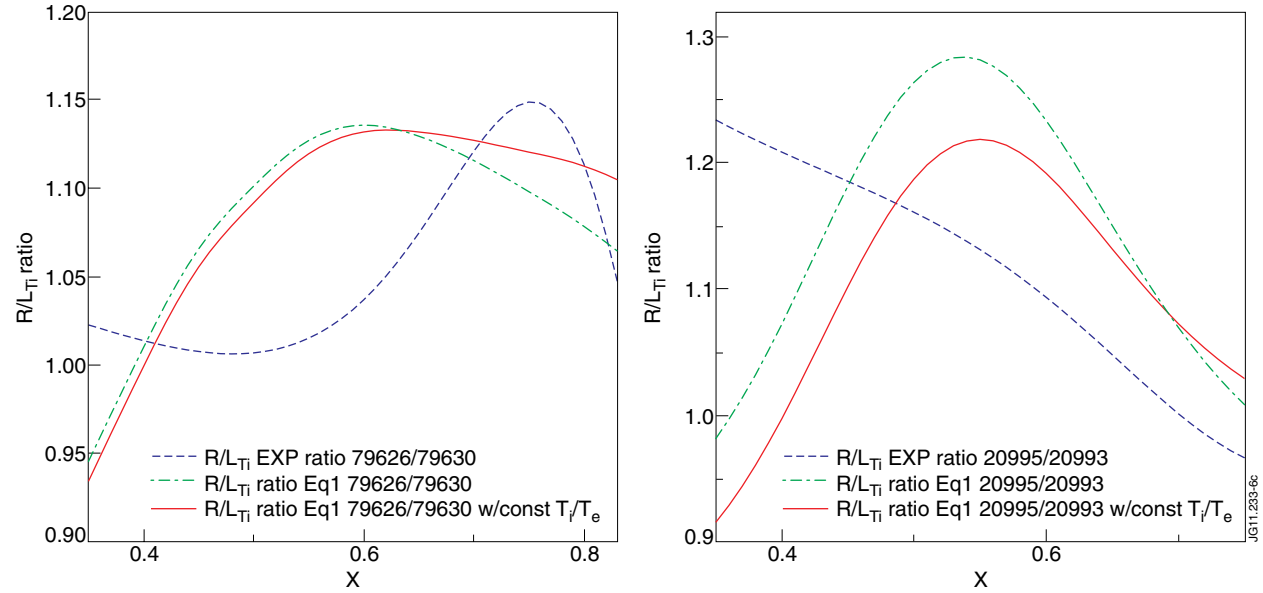

Figure 6: R/L_{Ti} experimental ratios compared with the analytical linear thresholds ratios (from equation 1) for JET Pulse No's: 79626/30 (left panel) and AUG 20993/95 (right panel).

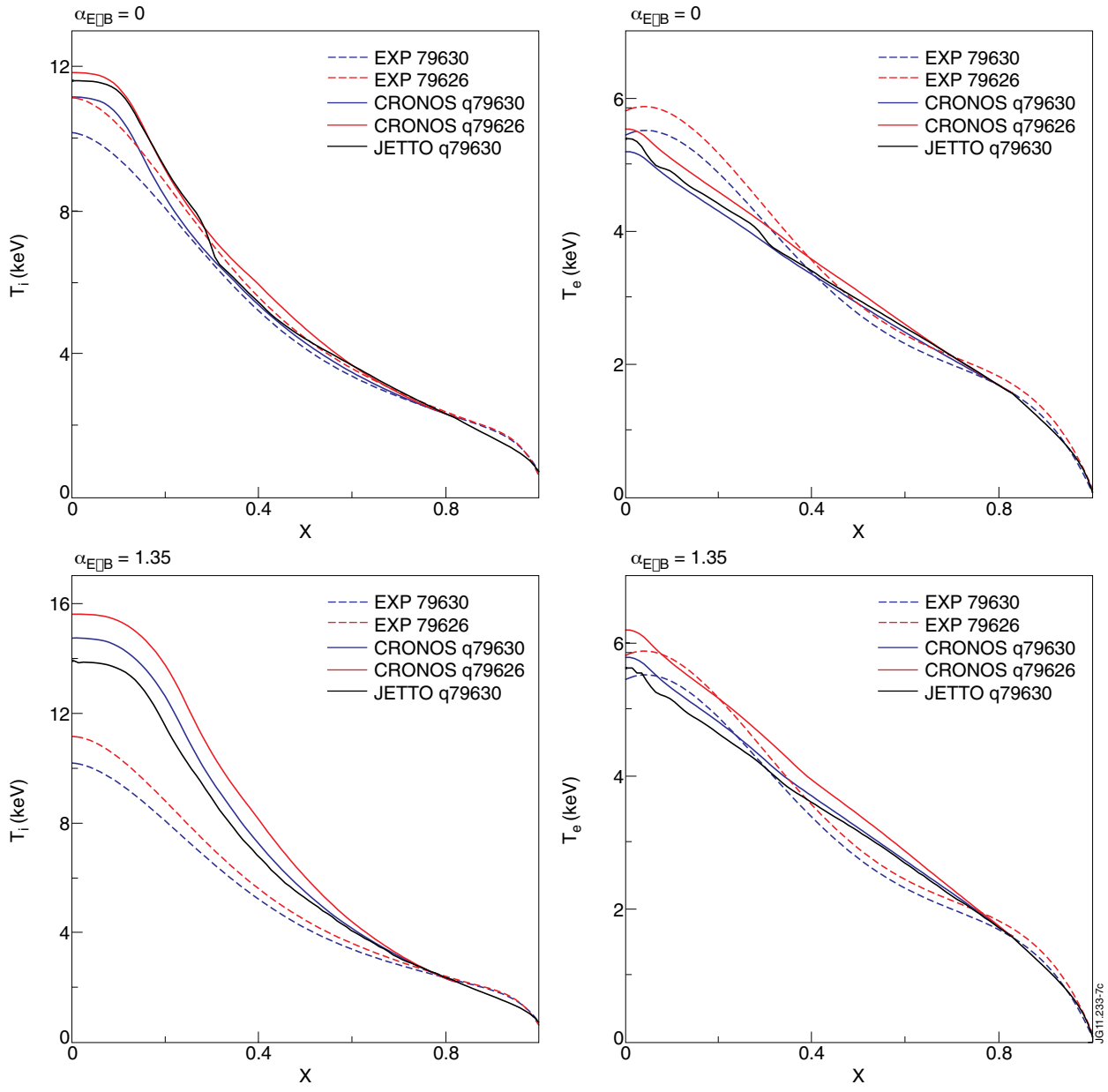

Figure 7: Results of heat transport only GLF23 simulations for JET Pulse No: 79630, comparing q-profile inputs from both Pulse No's: 79630 and 79626. T_i profiles are on the left column. Te profiles are on the right column. Results with both no E×B suppression (top row) and full E×B suppression (bottom row) are shown. JETTO/GLF23 simulation results are also shown, to benchmark the CRONOS/GLF23 results.

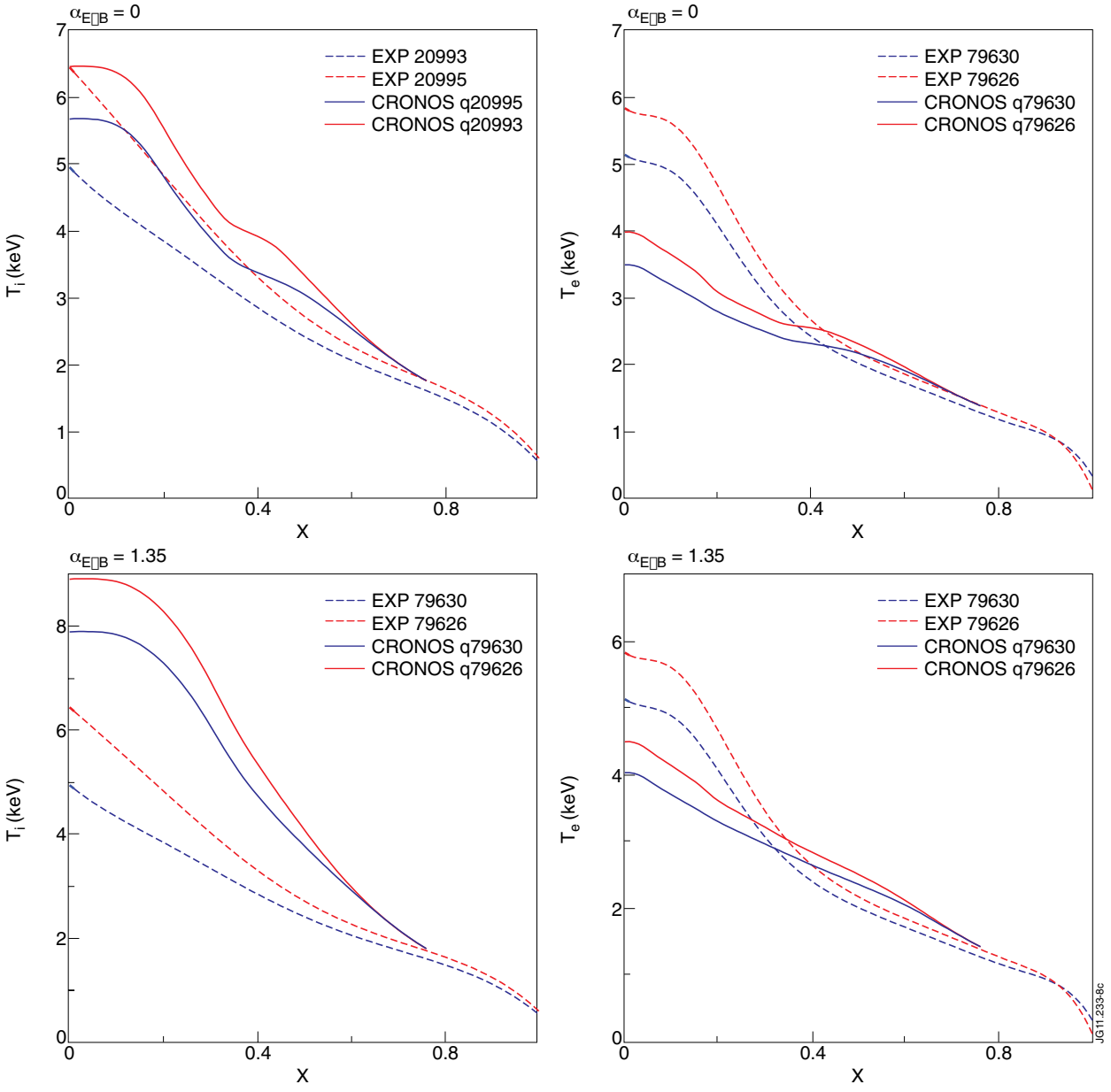

Figure 8: Results of heat transport only GLF23 simulations for AUG 20995, comparing q-profile inputs from both 20995 and 20993. T_i profiles are in the left column. Te profiles are in the right column. Results with both no E×B suppression (top row) and full E×B suppression (bottom row) are shown.

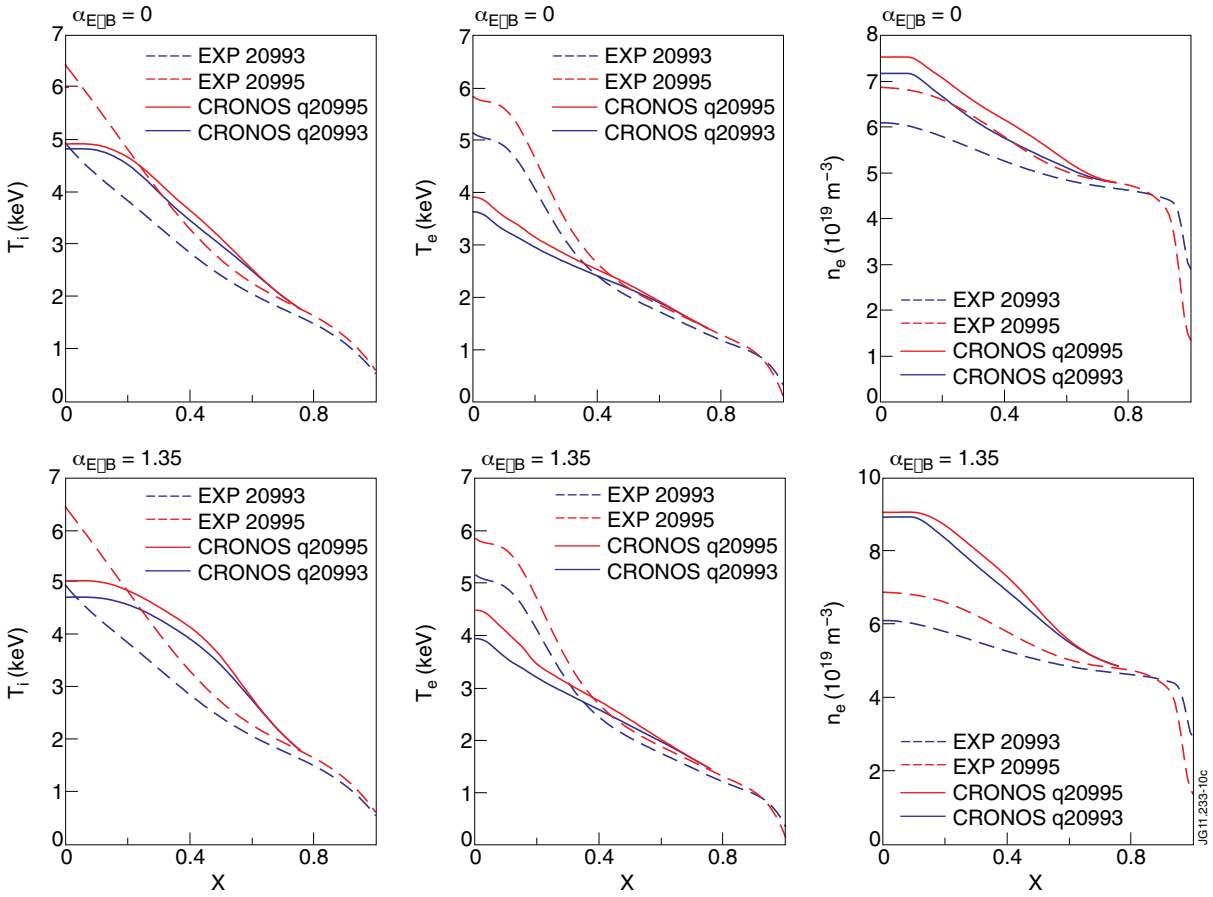

Figure 9: Results of combined heat and particle transport GLF23 simulations for JET Pulse No: 79630, comparing q-profile inputs from both Pulse No's: 79630 and 79626. T_i profiles are in the left column. Te profiles are in the center column. ne profiles are in the right column. Results with both no E×B suppression (top row) and full E×B suppression (bottom row) are shown.

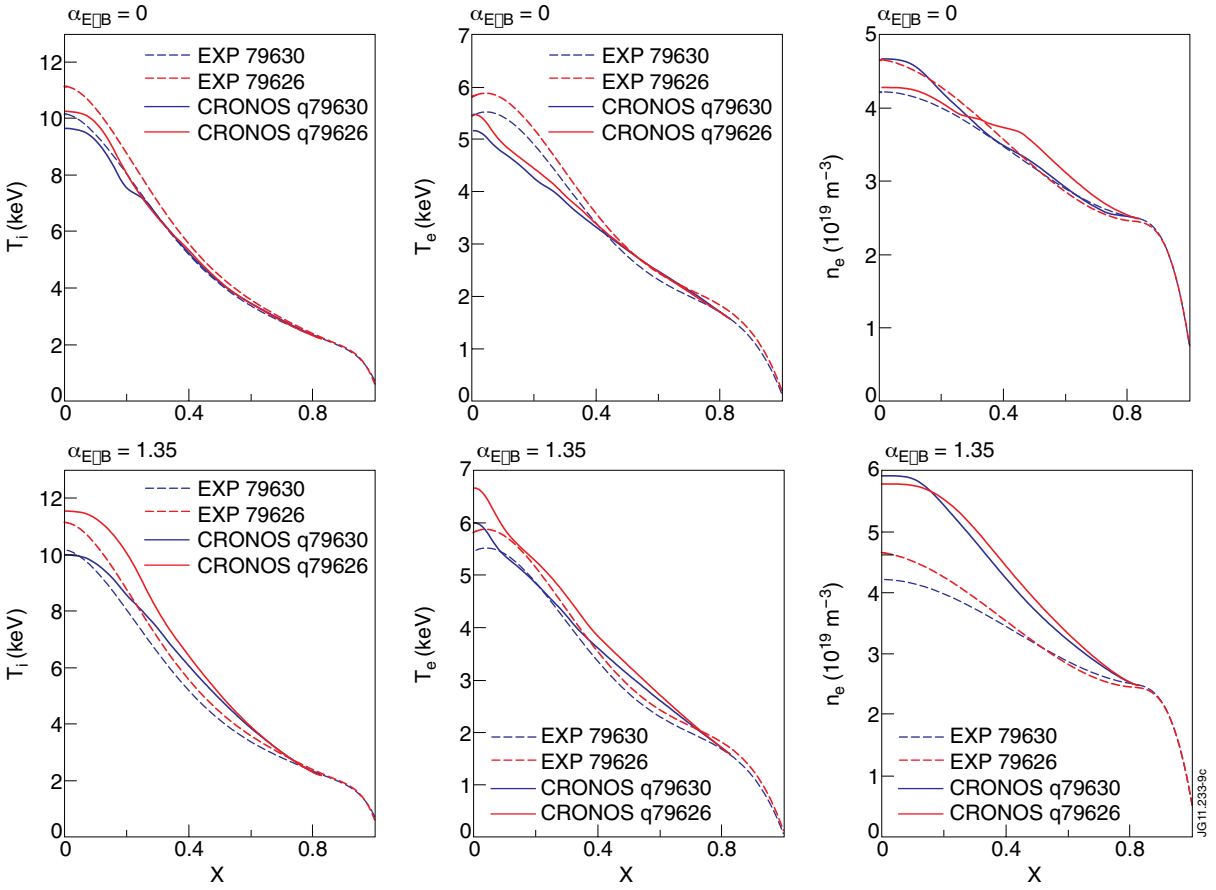

Figure 10: Results of combined heat and particle transport GLF23 simulations for AUG 20995, comparing q-profile inputs from both 20995 and 20993. T_i profiles are in the left column. T_e profiles are in the center column. n_e profiles are in the right column. Results with both no ExB suppression (top row) and full ExB suppression (bottom row) are shown.

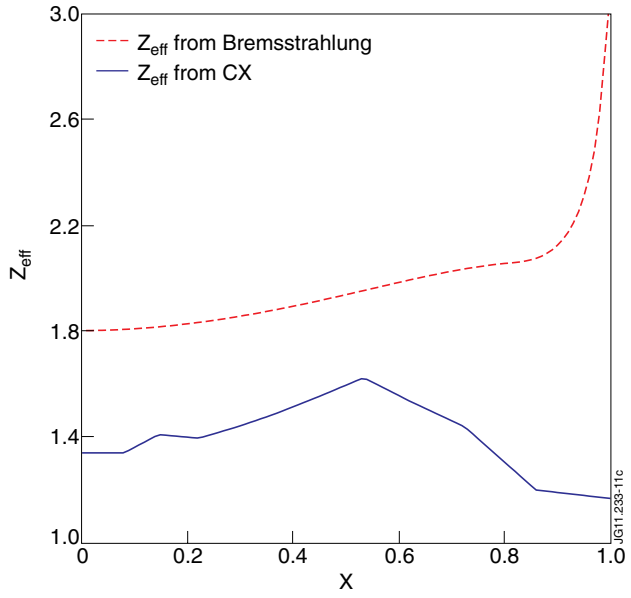

Figure 11: Comparison of Z_{eff} profiles for JET Pulse No: 79630 averaged between 7.14-7.64s, both from line averaged Bremsstrahlung and an assumed profile, and from carbon concentration CX measurements

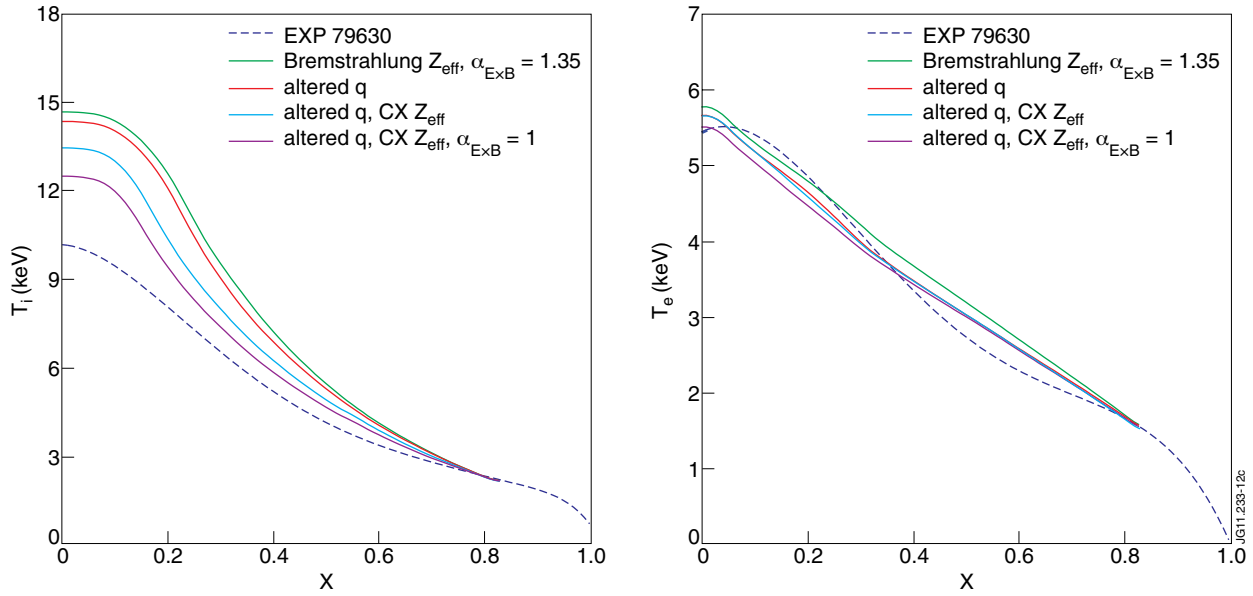

Figure 12: Results of heat transport GLF23 simulations for JET 79630, testing the sensitivity of the results to Z_{eff} and the α_{ExB} parameter. Progressive results for T_i (left panel) and T_e (right panel) are shown where the experimental profile is compared to: the original 79630 simulation with Bremsstrahlung Z_{eff} and α_{ExB} = 1.35, a simulation where the q-profile is substituted with the q-profile obtained with lowered Z_{eff} profiles, additionally reducing Z_{eff} itself in the predictive simulation to the CX measured Z_{eff} profile, and finally additionally switching the α_{ExB} parameter to 1.

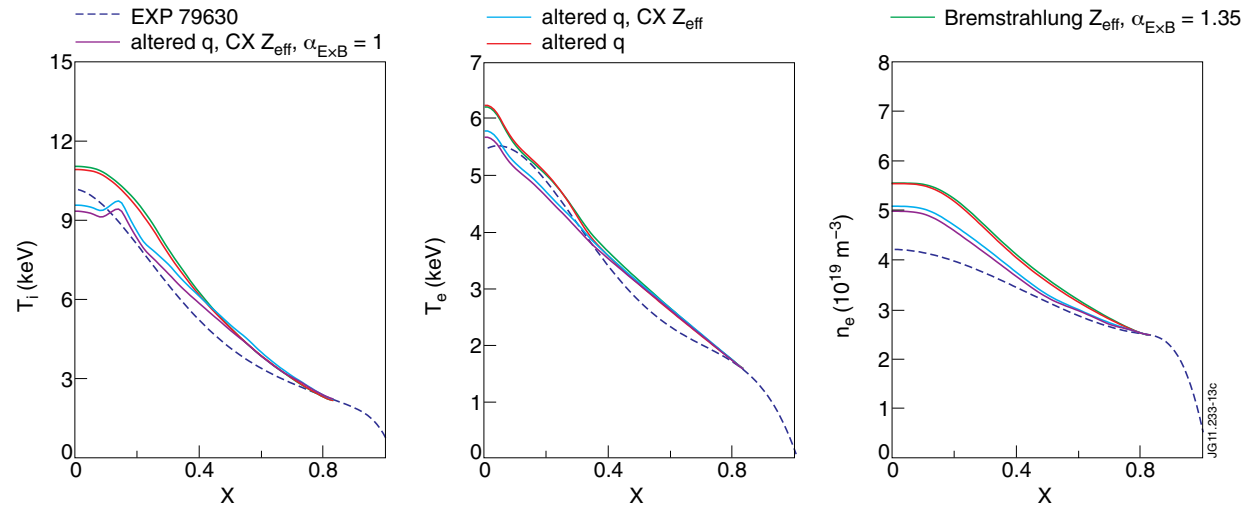

Figure 13: Results of combined heat and particle transport GLF23 simulations for JET 79630, testing the sensitivity of the results to Z_{eff} and the α_{ExB} parameter. Progressive results for T_i (left panel), T_e (center panel), and ne (right panel) are shown where the experimental profile is compared to: the original 79630 simulation with Bremsstrahlung Z_{eff} and α_{ExB} = 1.35, a simulation where the q-profile is substituted with the q-profile obtained with lowered Z_{eff} profiles, additionally reducing Z_{eff} itself in the predictive simulation to the CX measured Zeff profile, and finally additionally switching the α_{ExB} parameter to 1.

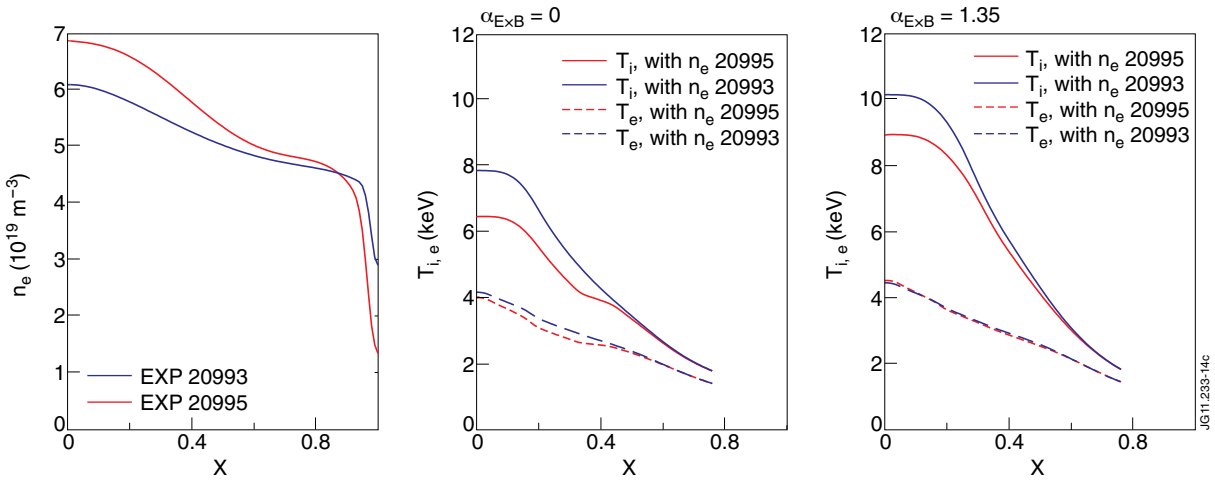

Figure 14: Comparison of AUG 20995 heat transport simulation with GLF23, with different prescribed n_e profiles. The dashed lines correspond to simulations with n_e from 20995, and the solid lines to n_e from 20993. The prescribed ne profiles are seen in the left panel, the temperature profiles without E×B suppresion in the center panel, and the temperature profiles with full E×B suppresion in the right panel.

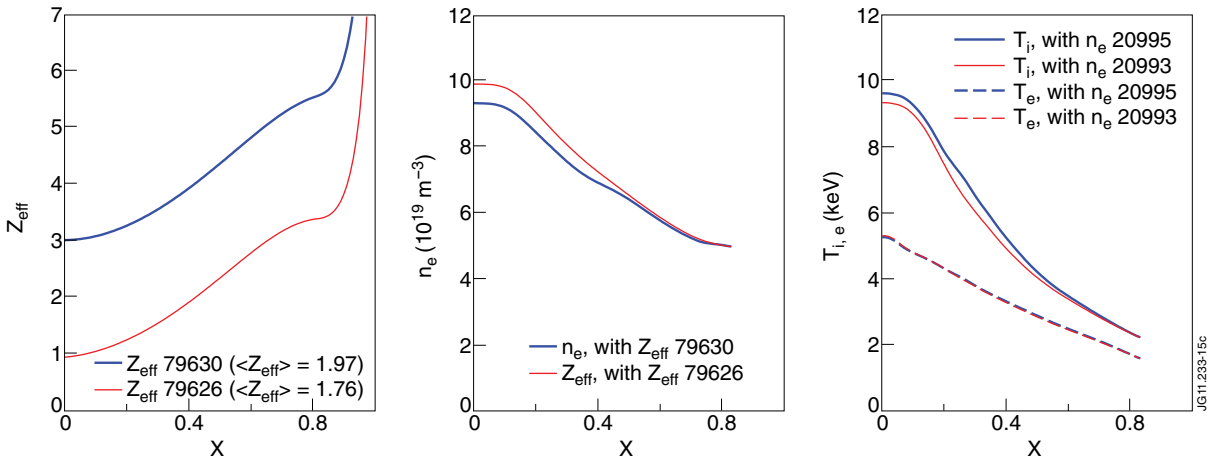

Figure 15: Comparison of JET Pulse No: 79630 combined particle and heat transport simulation with GLF23, without E×B suppression. The dashed lines correspond to simulations with Z_{eff} from Pulse No: 79630, and the solid lines to Z_{eff} from Pulse No: 79626. The prescribed Z_{eff} profiles are seen in the left panel, the density profiles in the center panel, and the temperature profiles in the right panel.

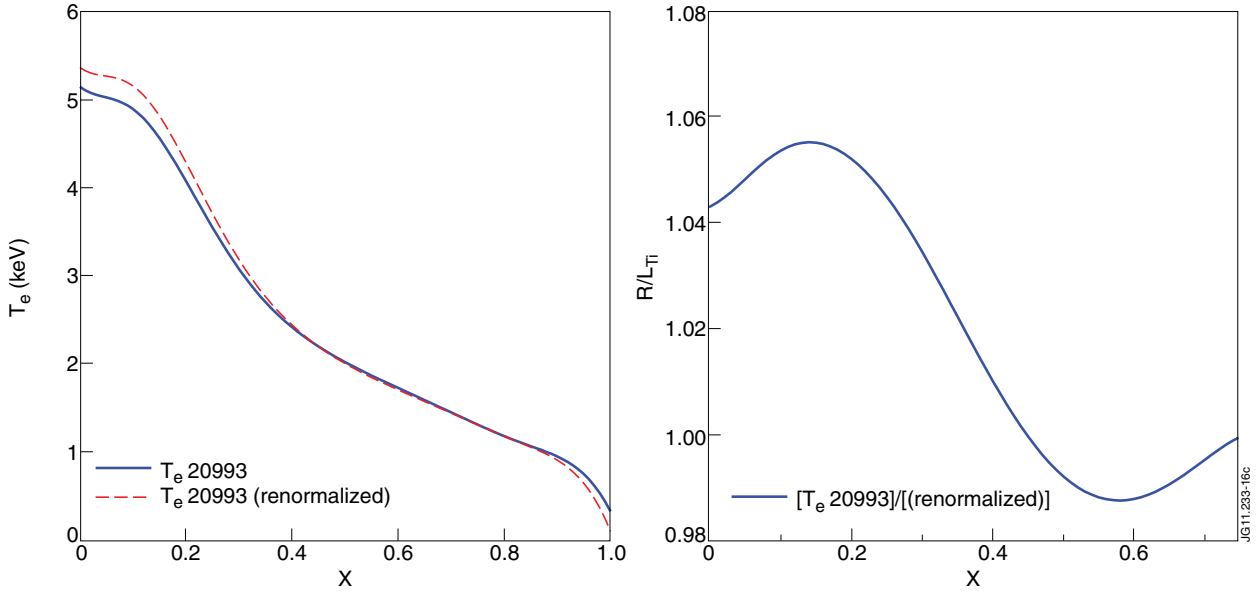

Figure 16: Comparison of AUG 20993 and 20995 T_e profiles, with the 20995 profile normalized to the 20993 GLF23 boundary condition at x = 0.76. The T_e profiles themselves are seen in the left panel, and the ratio between the profiles in the right panel.

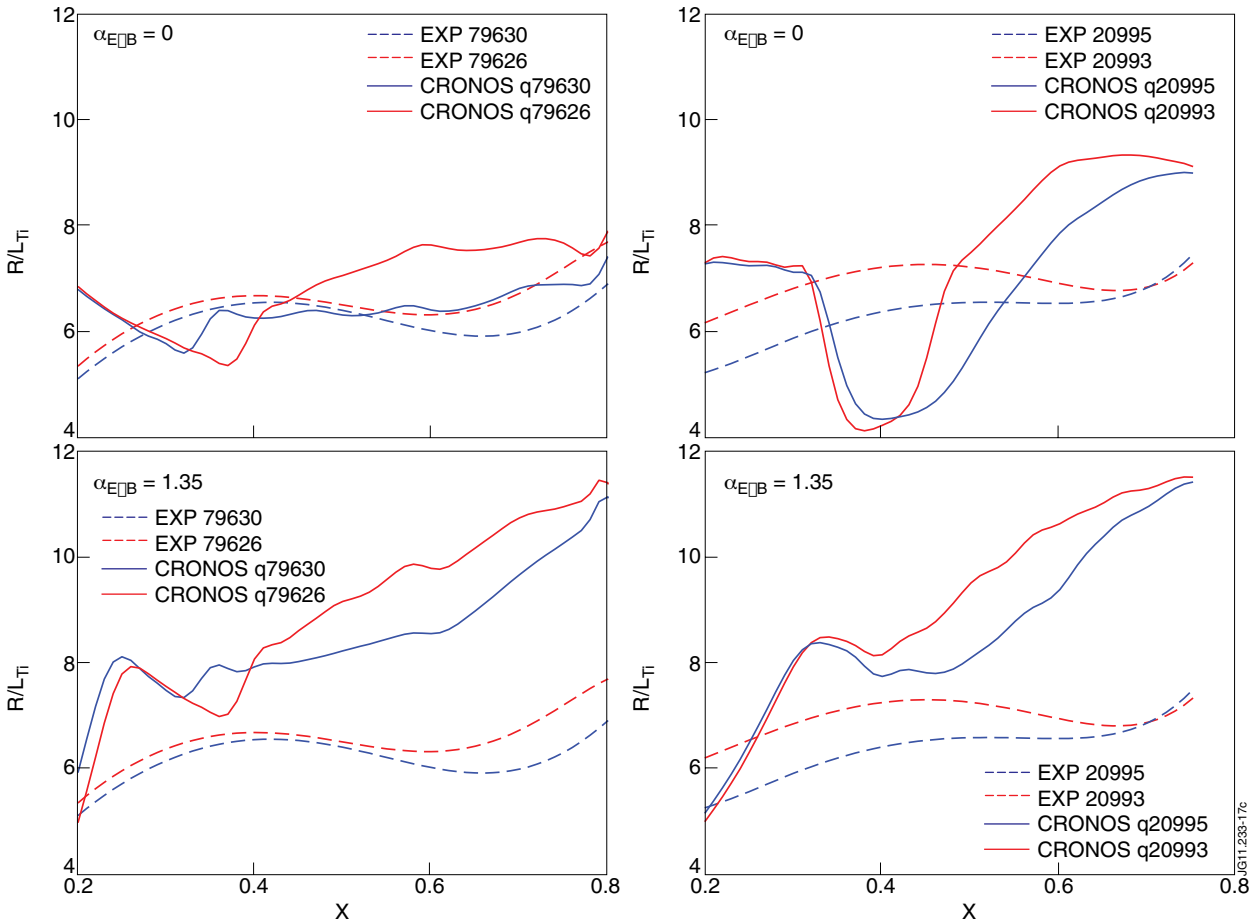

Figure 17: Comparison of R/L_{Ti} GLF23 predictions following q-profile substitution. Results are shown for the JET pair (left column) and the AUG pair (right column) both with (upper row) and without (lower row) the inclusion of E×B suppresion.

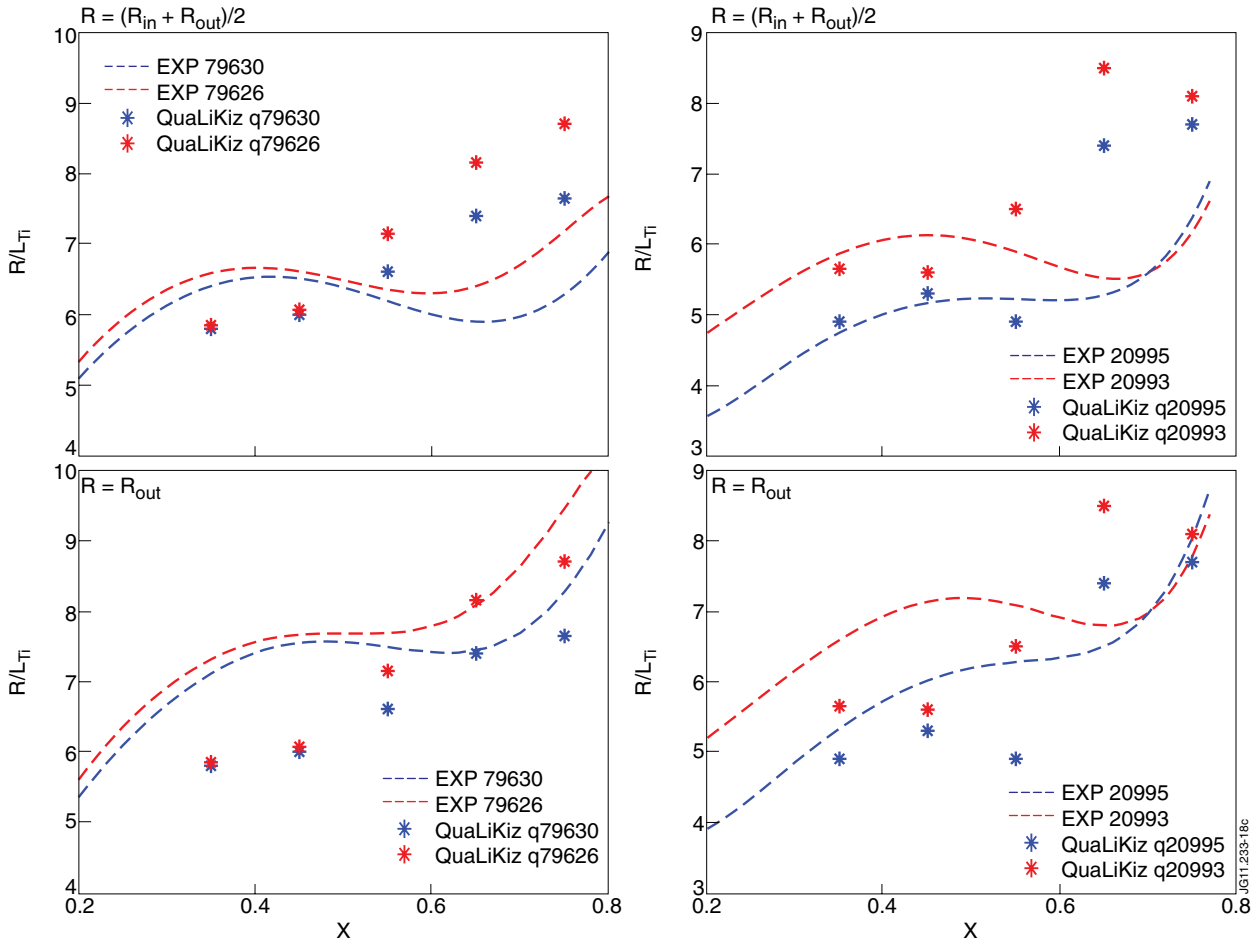

Figure 18: Comparison of R/LTi QuaLiKiz predictions following q-profile substitution. Results are shown for the JET pair (left column) and the AUG pair (right column). In the upper row the experimental gradients are calculated taking the radius as the average of the low-field side and high-field side. In the lower row the gradients are defined from the flux surfaces on the low-field side.

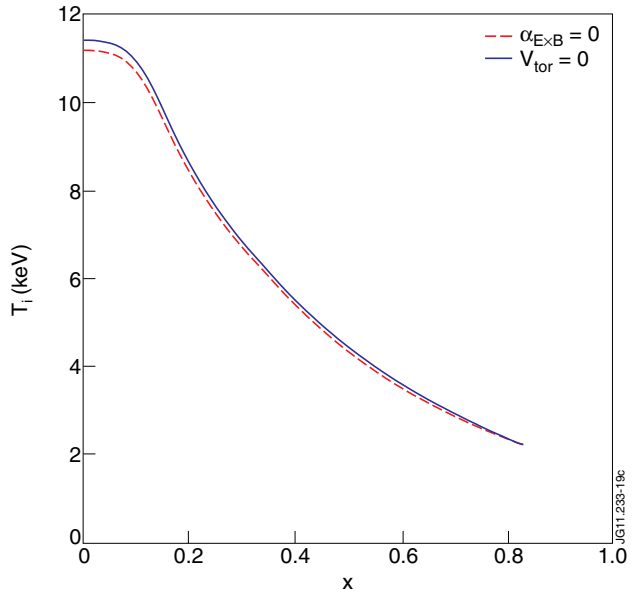

Figure 19: JET Pulse No: 79630 GLF23 heat transport only simulations, comparing a case with $\alpha_{E\times B} = 0$ in the ExB suppression model, and a case with the rotational profile set to zero, thus also removing the parallel velocity shear destabilization.